Chapter 5

Future work

5.1 Refinements to the present work

As discussed in Section 3.5.4, some fraction of the measured thresholds may represent stimulation of dendrites rather than axons. Since both axons and dendrites share the same basic cylindrical geometry, the identity of the target little effects the primary result of this thesis. Still, a more definitive statement about the stimulation target could be made if the stimulating and recording clusters were placed further apart than the largest dendritic spreads, perhaps 1mm or more. In the present experiments the cluster separation was kept small to reduce the sensitivity of the measurement to imperfect vertical alignment of axons. At larger separations, the chances of recording from a cell whose axon ran through the stimulating cluster would be reduced. The experimental setup will soon be modified, however, to permit single needle recording (to better isolate cells) while stimulating through an electrode array. The modified setup should facilitate threshold measurements with large stimulating-recording electrode separations, so that the measurements described in Chapter 3 can be repeated under conditions in which dendrite stimulation would be highly unlikely.

5.2 Field direction

This thesis suggests that axon thresholds can be raised through a strategic choice of electrode geometry. Thresholds for the transverse bipolar geometry, however, were very sensitive to fiber position, only becoming substantially elevated relative to thresholds for monopolar or longitudinal bipolar stimulation when the fiber under study was well-centered between the electrode poles. Longitudinal fringing fields near the electrode poles provide the most plausible explanation for this threshold profile. Hence future *in vitro* experiments might endeavor to design novel electrode geometries with better field directionality and minimal fringing.

One candidate design inspired by previous work (Grumet, 1994) is shown in Fig-

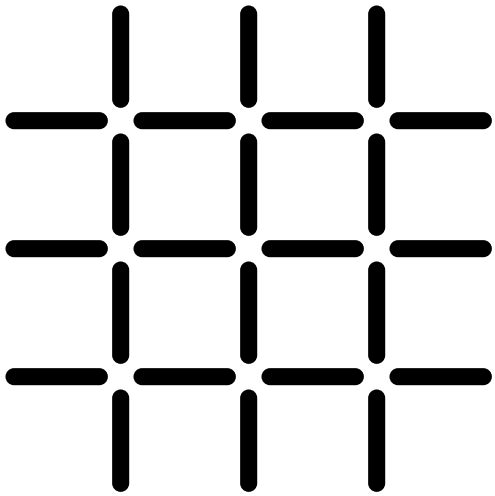

Figure 5.1: A stimulating electrode array resembling a tic tac toe board should provide better field uniformity than pairs of 10μm diameter disks for measuring thresholds versus field direction.

ure 5.1. Approximately uniform fields in the horizontal and vertical directions can be produced by connecting a stimulator across rows and columns of the array, respectively*. Longitudinal fringing fields will be a concern as before, though perhaps the elongated electrode geometry will reduce this fringing. Computer simulations or physical models might be employed to solidify qualitative notions about how much longitudinal fringing is to be expected for a particular electrode geometry.

Showing that axon thresholds depend on field orientation *suggests* a strategy for bypassing axons, but it does not *validate* this approach. Excitation thresholds for axons must ultimately be compared with thresholds for other retinal elements such as pre-synaptic cells or the ganglion cell's peri-somal region (i.e. the soma or axon hillock or initial segment) under comparable conditions. Responses originating in pre-synaptic elements can be distinguished from direct ganglion cell excitation by examining response latencies and using synaptic blockers like cadmium and APB†. To measure peri-somal thresholds, the location of the soma must first determined. This can be done coarsely by recording from the cell's axon and then probing the retina with

*Open-circuited electrodes can distort the stimulating field, as discussed in Section 4.1.1. Hence the actual field distribution may be more complex, depending on the relative sizes of the tissue and interface impedances.

†APB is an abbreviation for 2-amino-4-phosphonobutyrate, which blocks synapses in the retinal ON channel.

a spot of light to find the cell's receptive field center (Jensen et al., 1996). Further refinement of this estimate might be achieved with a tissue stain after threshold measurements are complete, provided that the cells are distributed sparsely enough that the target of stimulation can be unambiguously identified. Performing these measurements will require additional optical equipment not present in the current experimental apparatus.

5.3 Pulse duration

As discussed in Section 1.2.3, Greenberg (1998b) has found that stimulation targets depended on the duration of the stimulation pulse. However, all but one of these measurements (the phosphene experiment) were performed with 1.5mm diameter electrodes which were placed far from the epi-retinal surface. Will the same arguments apply with smaller surface-residing stimulating electrodes, where field strength will vary rapidly with retinal depth? The work of Doty and Grimm (1962) and Humayun (1999) provide some evidence to the affirmative, since these studies placed electrodes on the retinal surface and used pulse durations which were 1ms or longer, and in neither case were axons stimulated at the lowest currents. This hypothesis, however, has not yet been examined systematically with a realistic electrode configuration. Future work could also be directed at experiments to test this.

5.4 Electrode size

Table 3.4 shows that a significant range of electrode areas was used in the literature. In Section 3.5.1 I noted that the unusually small stimulating electrode size used for this thesis might account for the unusually low excitation thresholds reported in Chapters 2 and 3. Are thresholds small for small stimulating electrodes and large for large electrodes? And if so, how do the threshold versus diameter functions compare for different retinal elements? It may be that different electrode sizes stimulate different targets, in which case electrode size could be used as a tool for selectivity.

These questions can be answered experimentally using stimulating electrode array techniques. For example, a series of arrays with a range of disk diameters could be produced, with each array containing electrodes of one size. Several experiments could then be performed with each electrode size, and average thresholds compared for the different sizes. Alternatively, a range of electrode sizes could be fabricated on the same array. Measurements of the threshold versus diameter function for a particular element may prove problematic, however. On a first glance, the electrode pattern in Figure 5.2a would appear to be just the tool for the job. Using this type of pattern, thresholds could be measured with the stimulator connected between the central electrode and a distant return, then using the parallel combination of the central electrode and first ring, and so forth. Unfortunately, unused electrodes may

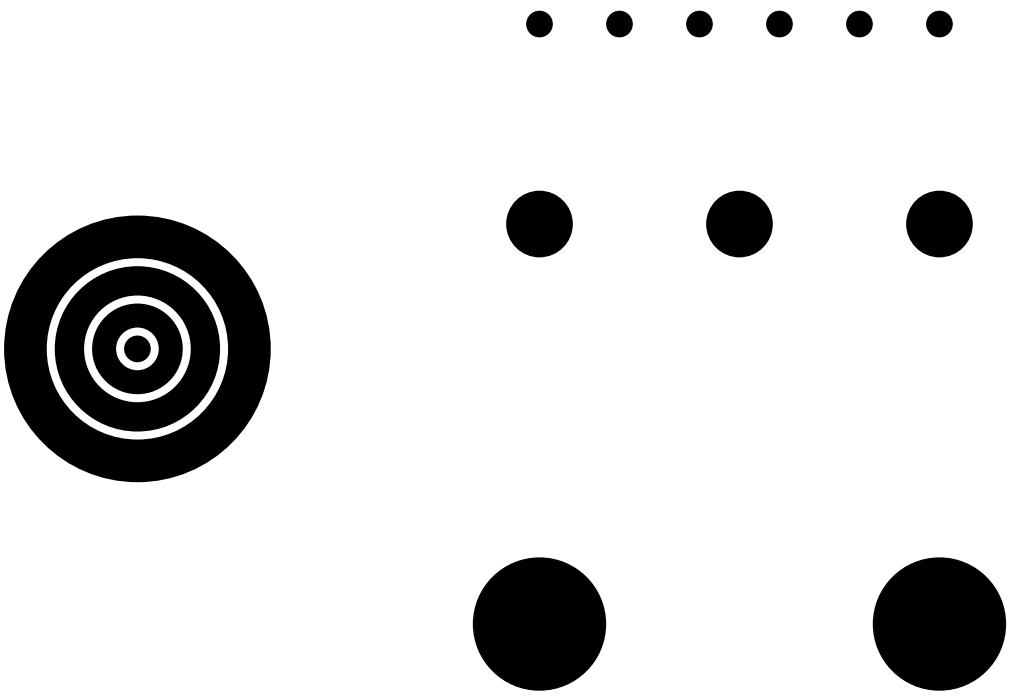

(a) (b)

Figure 5.2: Array patterns for measuring thresholds versus electrode diameter. (a) A concentric ring electrode could be used to measure thresholds for several electrode diameters, but field distortion from unused electrodes will probably confound the results. (b) An array with several electrode sizes can be used to compare thresholds from the same retina but at different stimulation sites.

significantly distort the stimulating field as noted in Chapter 4. Hence stimulating fields obtained with central electrode alone will be spatially smoothed by the large surrounding rings, and will probably have higher threshold currents than would the same electrode surrounded by insulator only. This ambiguity can be avoided with arrays containing simple disks of different sizes which are placed reasonably far apart (a few electrode diameters), as in Figure 5.2b. Thresholds for a range of different sizes can be measured on the same retina, but the group of neurons stimulated will be different for each electrode.

Appendix A

Thresholds for *In Vitro* Human Retina

On August 18, 1999, a sample of living human retina was made available for study. The sample came from the eye of a patient at the Massachusetts Eye and Ear Infirmary with cancer of the lacrimal gland extending throughout the eye socket. The patient's eye was removed as part of the cancer treatment. The patient was aged 77, male, with 20/25 acuity and no known visual problems.

In surgery, the entire eye socket with surrounding bone was removed. The intact eye was then removed from the socket, placed in normal saline solution, and rushed to the laboratory where it was opened and the retina dissected free. The retina was placed in oxygenated Ames' medium (pH 7.3-7.4) approximately one hour after removal of the eye from the patient.

Single unit spike thresholds were measured exactly as described in Chapter 2, except that in this case the retina patch was cut from the periphery. A total of 53 thresholds were measured for units picked up by six different recording electrodes. Monopolar thresholds were similar to those found in rabbit, ranging from .2 to 1.3μA.

A partial monopolar threshold map was made for one unit. This map is shown in Figure A.1.

Graded potentials made it impossible to determine thresholds at many of the stimulating electrodes. However, the low variation in thresholds along the third column of the map (particularly among the upper five electrodes) suggests that the alignment of the fiber under study was close to vertical. Furthermore, the fourth column contained two large thresholds which suggested that the fiber was to its left.

Bipolar thresholds were measured with pairs of electrodes spaced 50μm apart in the same row (horizontal alignment) or column (vertical alignment). The current source was connected to the bipolar electrode pairs in a manner analogous to that described in Chapter 3, with the + terminal of the current source connected to the electrode with lower monopolar threshold. This was verified by the fact that spikes always immediately followed the end of the stimulus phase which drove this electrode

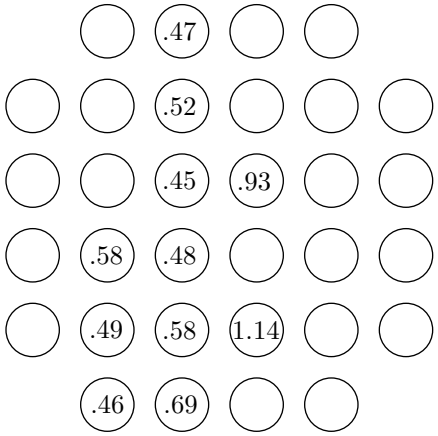

Figure A.1: Monopolar threshold map for *in vitro* human retina. Thresholds are in μA

Normalized thresholds	
Vertical	Horizontal
1.02	1.39
1.11	1.46
1.16	1.51
1.22	1.54
	1.56
	1.64

Table A.1: Normalized thresholds for horizontal and vertical bipolar stimulation.

cathodically (see Chapter 3).

Normalized bipolar thresholds are listed in Table A.1. Even though the surface separation between fiber and electrodes was uncertain, it is clear that normalized thresholds for horizontally aligned stimuli were greater than those for vertically aligned stimuli.

These results suggest that:

- The unusually low thresholds reported in Chapter 3 are not particular to rabbit; fibers at the surface of human retina can also be stimulated at sub-microampere currents. The discrepancy with thresholds for human phosphene perception, which were several hundred microamperes or larger, cannot be accounted for by retinal anatomy differences in the two species.

- Fiber thresholds depend on field orientation in human retina just as they do in rabbit retina. Thresholds are larger for fields running perpendicular to fibers

than for fields running parallel to fibers.

Appendix B

Instrument Designs

B.1 Introduction

To make the measurements documented in earlier parts of this thesis I designed and built several specialized electronic instruments. These instruments consist of: a current source which delivers stimuli to the retina, a bank of nerve response amplifiers which simultaneously monitor the activity at eight sites on the retina, and a pair of amplifiers which monitor the electrode current delivered (which, in principal, should be equal to that requested of the source) as well as the voltage required for delivery. Functional block representations of the new instruments are shown in bold outline in the diagram of Figure B.1. This appendix details their designs.

B.2 Stimulator design

A block diagram of the stimulator is shown in Figure B.2. The circuit consists of several subsystems, including an isolator which decouples the computer D/A ground from the current source ground, an active filter to reduce high frequency noise added to the signal by the isolator, a switching network to decouple the still somewhat noisy signal from the current source when the stimulator is not in use (this reduces noise picked up by the response amplifiers), and the current source itself. The details of these subcircuits will now be considered in turn, followed by a summary of the stimulator's measured performance.

B.2.1 Isolator

The current source ground is isolated from the computer D/A ground using a Hewlett-Packard HCPL-7820 chip, which converts input voltages to a stream of digital bits, transmits the stream optically across an electrical isolation barrier and then converts the bits back to an analog voltage on the output side. Isolation implies that almost

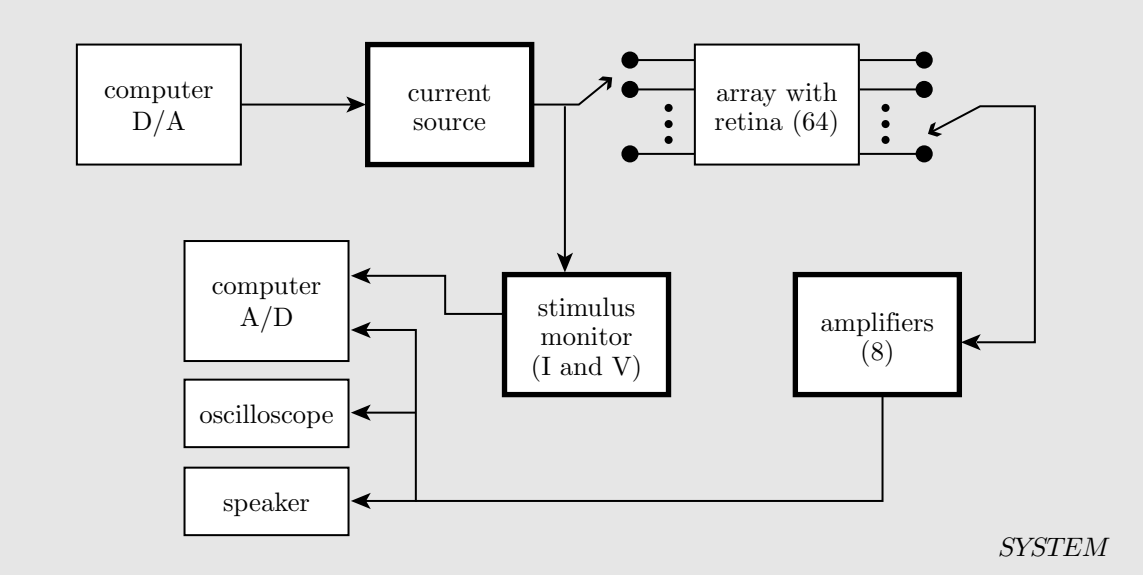

Figure B.1: Block diagram representing signal flow in the experimental apparatus.

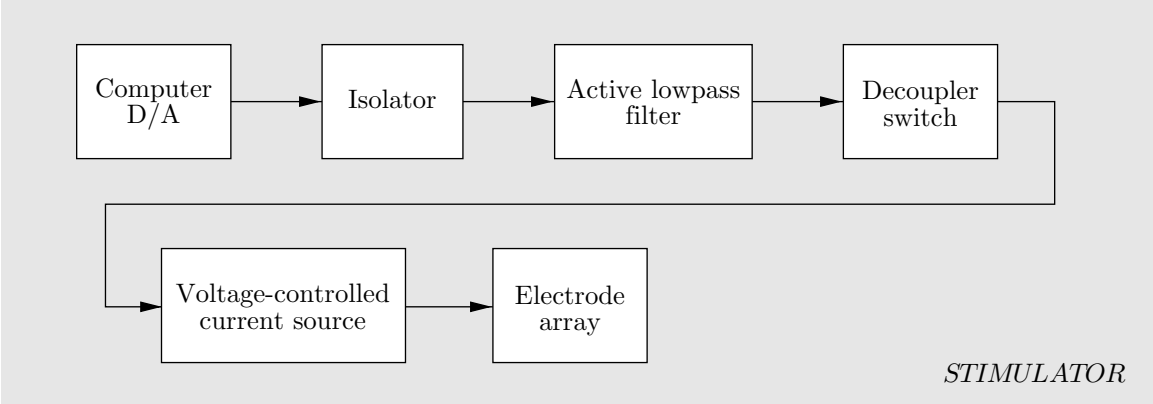

Figure B.2: Block diagram of the stimulator.

ISOLATOR

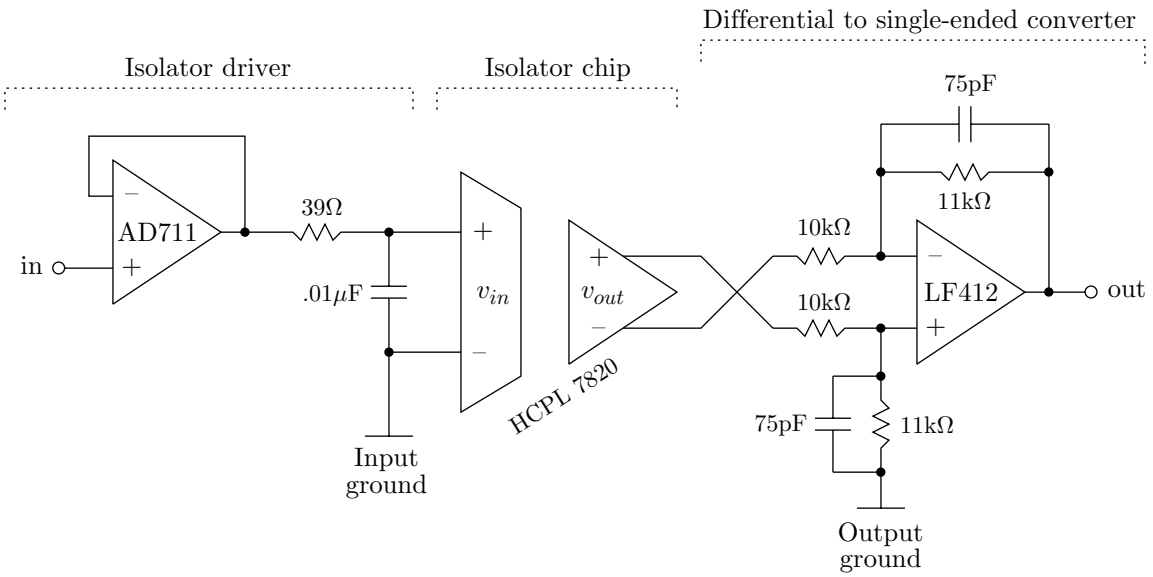

Figure B.3: Schematic diagram of isolator driver, isolator, and differential to single-ended converter.

no electric current will flow in loops passing through the isolation barrier, so that the stimulator output can be treated as a floating source.

The stimulator command voltage generated by the computer is coupled through a 50:1 resistor divider to the isolator circuit illustrated in Figure B.3 (the resistor divider is not shown in the Figure). The first section of the circuit, labeled Isolator driver, consists of an op-amp buffer and a passive lowpass filter. The filter, used on the suggestion of the 7820 data sheets, stabilizes the switched-capacitor filters at the input of the chip, as well as acting as an anti-aliasing filter. Referring to second section of Figure B.3, labeled Isolator chip, the HCPL-7820 has the following characteristic

$$v_{out} = 8v_{in}; \qquad -200\text{mV} \leq v_{in} \leq +200\text{mV}.$$

Within the indicated range of input voltages, Hewlett-Packard guarantees the differential gain of 8 to within 3%. The resistor divider mentioned above (not shown in Figure B.3) scales the ±10 volt output range of the computer's D/A board to the acceptable HCPL-7820 input range. The third section of the isolator circuit converts

the differential output of the HCPL-7820 to a single-ended signal. The differential to single-ended converter has a low frequency gain of 11/10 which rolls off above 200kHz.

B.2.2 Lowpass filters

The output of the 7820 is substantially contaminated with noise, primarily near 500 kHz, which is generated by a chopper-stabilized amplifier inside the chip. Unfiltered, this noise is roughly 100mV peak-to-peak at the output, or 12.5 mV peak-to-peak referred to input. Considering the peak allowable input voltage of 200 mV, this noise represents a severe limitation on the useful range of signals which can be passed through the 7820.

Since this noise is in a slightly higher band than frequencies of interest (stimulation pulse widths no shorter than 20μs are anticipated), it can be substantially filtered out with four poles of lowpass in the 100kHz to 200kHz range. The first pole is provided by the differential to single-ended conversion circuit of Figure B.3. The fourth pole is provided by a passive RC formed through the analog switch in the decoupler circuit (see Figure B.5) by the 1kΩ resistor and the 680pF capacitor.

The second and third poles are provided by an active, lowpass, two-pole Bessel filter. The filter is implemented using the circuit of Figure B.4 with R_1=13.3kΩ, C_1=47pF, R=37.4kΩ, and K=1.267. A Bessel-type filter provides a compromise between a steep pass-band (to reject the isolator noise) and good time domain performance (preserving the shape of rectangular current pulses). The 3dB cutoff frequency of the filter is given by $f_c = 1/2\pi R_1 C_1 f_n$, where $f_n = 1.272$ (Horowitz and Hill, 1989), yielding a cutoff of 200kHz.

The input-referred isolator noise is reduced by the lowpass filters to 1.25mV pk-pk. Referenced to the input of the stimulator (i.e. to the input of the resistor divider preceding the isolator section), this noise is about 63mV pk-pk.

B.2.3 Decoupler circuit

Even with the reductions provided by the lowpass filters discussed above, an appreciable amount of noise is still present in the signal driving the controlled current source. Out of concern that this noise might distort the recorded neural signals, a means was provided to decouple the noisy isolator output from the current source input when not passing stimulation current. This decoupler circuit is illustrated in Figure B.5.

An analog switch (MC14066) is used to either connect or disconnect the active filter output from the voltage-controlled current source. When passing stimulation current, the switch is closed by applying a logic HIGH (5V) to the On/Off terminal of the stimulator. Conversely, the switch is opened when no stimulation current is desired by applying a logic LOW (0V) to the ON/OFF terminal.

The switch control signal, provided by the computer, is isolated from the controlled current source ground using the NEC2501 light-emitting diode/phototransistor pair.

ACTIVE LOWPASS FILTER

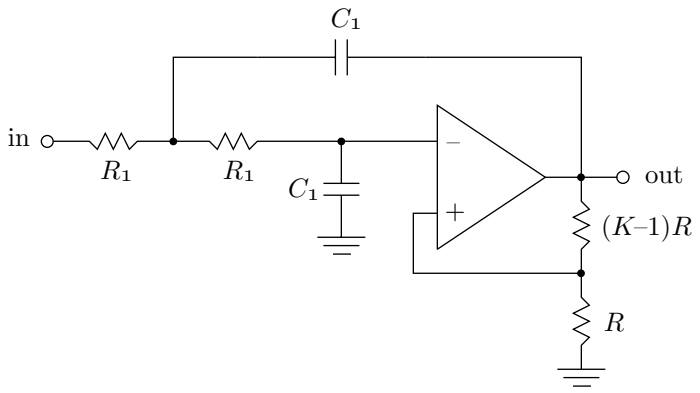

Figure B.4: Schematic diagram of a generic 2-pole active lowpass filter.

A more complex isolation amplifier such as the HCPL-7820 is not needed in this case since the signal to be isolated is digital. The ECL inverter formed by Q1 and Q6 supplies about 4mA to the NEC2501 input when the ON/OFF terminal is at 5 volts*, which in turn gets transferred to the output with a (measured) ratio of about two. To keep the switching speed as fast as possible, a relatively low 100Ω resistor is placed on the 2501's output. Multiplied by a current step of about 8mA, this resistance provides a total voltage change of just under 1V at the 2501's output during a logic transition. This small excursion is converted to a rail-to-rail transition (needed to drive the analog switch) using the emitter-coupled logic gate formed by Q3 and Q4 and an RTL inverter (Q5).

A 680pF capacitor is placed at the output of the analog switch in order to minimize the voltage "glitching" generated by charge dump accompanying logic transitions at the switch control input. This capacitor also forms a passive lowpass filter with the switch resistance, helping to reject isolator noise as mentioned in Section B.2.2. The 10kΩ resistor in parallel with the capacitor is used to hold the positive input of the VCCS op-amp near zero when the analog switch is open. With the switch closed, the cutoff frequency of the passive filter is 232kHz, assuming the "typical" switch resistance of 120Ω.

*An ECL inverter is used here rather than a simpler RTL inverter to avoid large changes in the total current demand on the power supply, averting possible stimulus artifact contributions via power supply coupling.

DECOUPLER

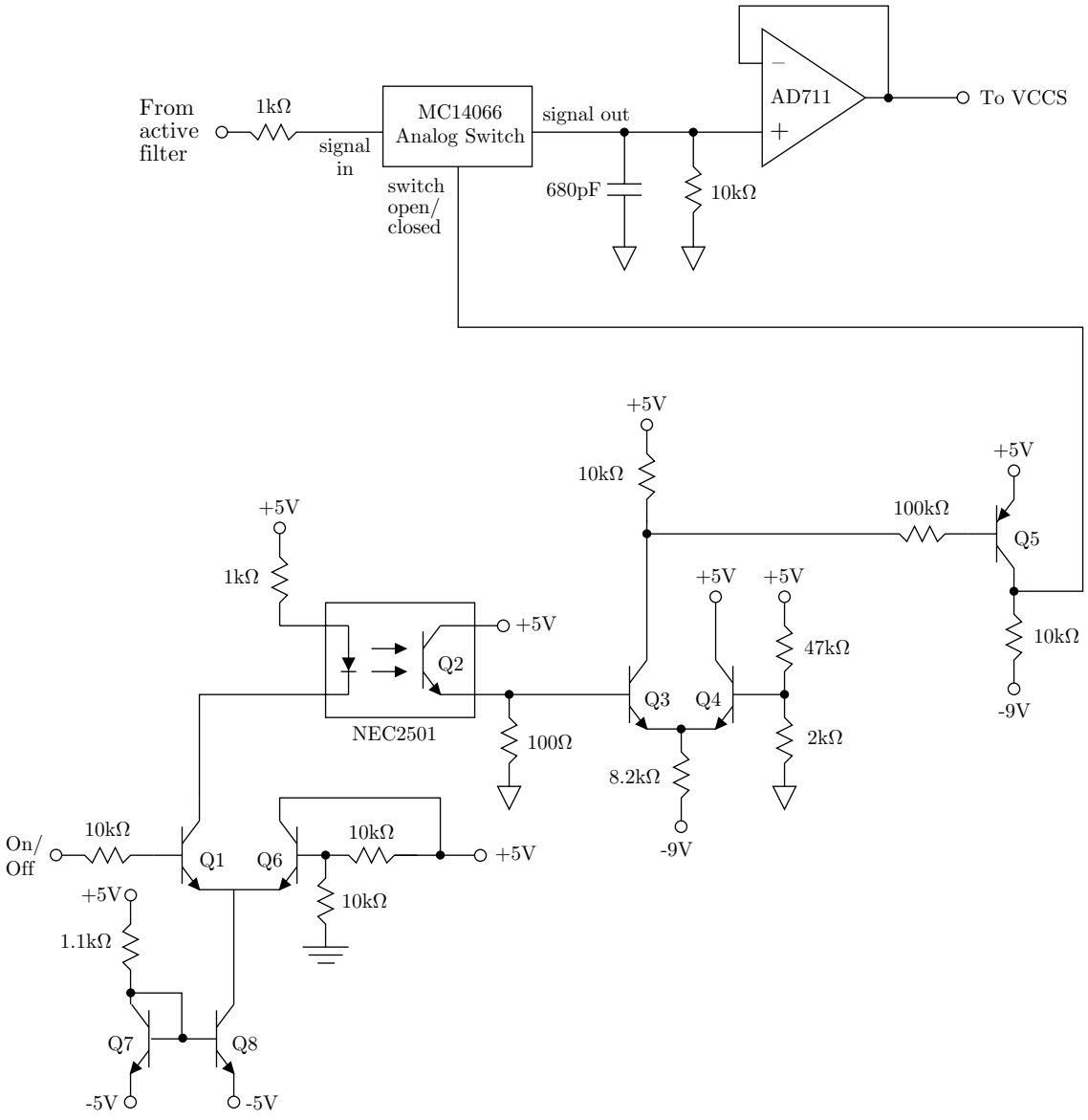

Figure B.5: Schematic diagram of circuit used to decouple the stimulator from the noisy isolator output.

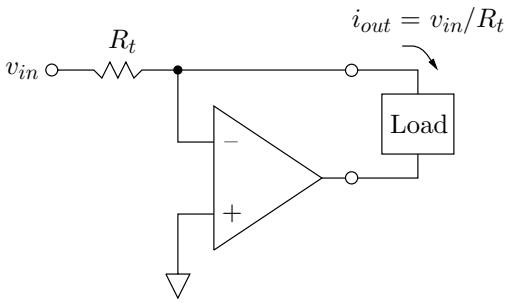

Figure B.6: Voltage-controlled current source topology.

Finally, to help minimize transients at the current source output upon switch opening or closing, two offset-trimming potentiometers are provided (not shown in the Figures). With the decoupler opened, the offset of the VCCS op-amp (AD711 in Figure B.7) is first zeroed using a trimpot connected directly to that op-amp. Then the switch is closed, and the offsets associated with the preceding amplifier and filter stages are zeroed by adjusting the trimpot connected to the isolator driver buffer (see Figure B.3). This procedure ensures that turning the switch on and off does not produce steps in the stimulation current when it is set to zero.

B.2.4 Current source

Essential topology

In its simplest form, the voltage-controlled current source (VCCS) used in the stimulator circuit may be drawn as in Figure B.6. If the operational amplifier output is not saturated or slewing, the current i_{out} through the load is

$$i_{out} = v_{in}/R_t.$$

The resistor R_t (the $_t$ is for *transconductance*) sets the ratio of input voltage to output current. One of three different values of R_t—10kΩ, 100kΩ, and 1MΩ–is selected by shorting together an appropriate pair of jumper posts on the stimulator circuit board.

Output circuit

A collection of resistors and capacitors are connected between the VCCS output and the stimulator output terminals. The significance of these elements, which are shown

VCCS

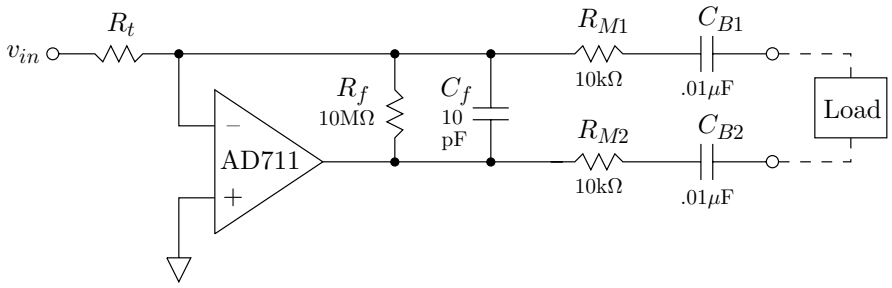

Figure B.7: Voltage-controlled current source and output network.

in Figure B.7, are now considered.

R_f and the C_B's

The capacitors C_{B1} and C_{B2} block DC and low-frequency currents from flowing through the electrodes. These are needed because sustained current can cause irreversible chemical reactions capable of destroying the electrodes or damaging the retina (Robblee and Rose, 1990). The total amount of unbalanced charge deliverable to the electrodes is approximated from the value of the capacitors and from the supply levels used to power the operational amplifier in Figure B.7. For example, if $C_{B1} = C_{B2} = .01\mu$F, and if the op-amp is powered by ± 9 volts, then at most the op-amp can deliver

$$\mathrm{Q} = \pm\frac{1}{2} \times .01\mu\mathrm{F} \times 9\mathrm{V} = \pm 45\mathrm{nC}$$

of unbalanced charge before it saturates. This charge is equivalent to a 1ms long pulse of 45μA, or a 10ms long pulse of 4.5μA.

The large resistor R_f provides feedback to stabilize the operational amplifier at DC. The value of R_f was chosen to be large enough to minimize shunt current away from the stimulating electrodes[†], but small enough that the DC gain ($-R_f/R_t$) provides reasonable stability in the face of the nonzero, drift-prone input offset voltage of the op-amp.

[†]The impedance of 10μm-diameter disks plated with platinum black, at time scales comparable with stimulation pulse widths, has a magnitude on the order of 100kΩ and a slight negative phase shift (see Figure B.23).

The output network will only deliver currents lasting less than about $R_f C_{B1}$ seconds (see section B.6). Given R_f, the value for the C_B's was chosen to keep the $R_f C_B$ product about two orders of magnitude above the width of the longest anticipated stimulation pulses (about 1ms duration).

The R_M's

The resistors R_{M1} and R_{M2} are used to measure the stimulation current flowing through the load. Since the voltage across these resistors is $i_{out} R_M$ when the load current is i_{out}, we can measure the voltage across the resistors to determine i_{out}. This provides a means to verify that the load is actually receiving the desired current. Measuring the voltage across *both* terminals of the current source provides a way to verify if and when it is behaving as an ideal two-terminal circuit element (see section B.5.2).

C_f

Placing the capacitor C_f as shown in Figure B.7 was found experimentally to eliminate a slight "jaggedness" appearing in the step response of the load current. The feedback provided by C_f apparently stabilizes the network at high frequency. The addition of C_f also increases the rise-time of the load current (see section B.6).

B.2.5 Performance specifications

Description	Value	Units	Note
Noise floor	∼63	mV	1
Maximum input	±10	V	2
Output Current to Input Voltage ratio	.2, 2, 20	μA/V	3
10% - 90% Rise time	2-7	μs	4
Output Voltage Limits	∼-7.3 and +7.9	V	5

Notes:

1. Measured at the input of the voltage-controlled current source, and referred to the stimulator input (i.e. the input to the voltage divider driving the isolator section).

2. The HCPL-7820 isolator gain is guaranteed to within 3% for input voltages between -200mV and +200mV. Since the stimulator input is divided down by

a factor of 50 before delivery to the isolator, as much as 10 volts positive or negative can be applied without compromising accuracy. Somewhat larger signals can be applied without damaging the isolator (see HCPL-7820 data sheets, from Hewlett-Packard). However, the isolator output will begin to clip when its input magnitude rises above 320mV.

3. The output current to input voltage ratio is set by a jumper labeled R_t which is located on top of the circuit board holding the stimulator.

   For a particular value of R_t, this ratio is calculated by multiplying $1/R_t$ and the product of the attenuator ratio (1/50), the isolator gain (8), the gain of the differential to single-ended converter (11/10), the gain of the Bessel filter (1.267), and the attenuation of the final lowpass filter which includes the switch (about 10/11).

4. The 10% - 90% rise time was determined by examining the voltage transient across R_{M2}. A 220 kΩ resistor was used as the load. The rise time varied with choice of R_t as follows. For R_t=10kΩ, the rise time was 7μs; for R_t=100kΩ, the rise time was 5.8μs; and for R_t=1MΩ, the rise time was under 2μs.

5. The output voltage limits of the current source are determined by the supply levels used to power the AD711 op-amp which implements the current source, and by the extent to which the AD711 can bring its output to these supply levels. According to the data sheets, for ±15 volt supplies, a typical AD711 can bring its output as high as +13.9V (1.1V below its positive supply) and as low as -13.3V (1.7V above its negative supply). Since the supply rails for this circuit are nominally ±9V, the output voltage limits are estimated as +7.9V and -7.3V (i.e. 1.1V below the positive supply and 1.7V above the negative supply, respectively). It is important to note, however, that the current source is powered by 9V alkaline batteries, whose terminal voltages may start slightly above 9V and will fall below 9V with time and use.

B.3 Stimulus monitor amplifier design

Two nearly identical amplifiers were built to monitor stimuli as they were delivered to the array. One of these monitors amplifies the voltage across a 10kΩ resistor in series with the load (labeled R_{M1} in Figure B.7), providing a measure of the current. The other monitor was usually used to track the voltage output of the current source op-amp (AD711 in Figure B.7). This voltage is dominated by the drop across the stimulating electrodes. In a few instances (see section B.5.2) the second monitor was used to measure the voltage drop across R_{M2}, allowing for simultaneous measurement of both current source branch currents.

A block diagram for one stimulus monitor is shown in Figure B.8. The monitor

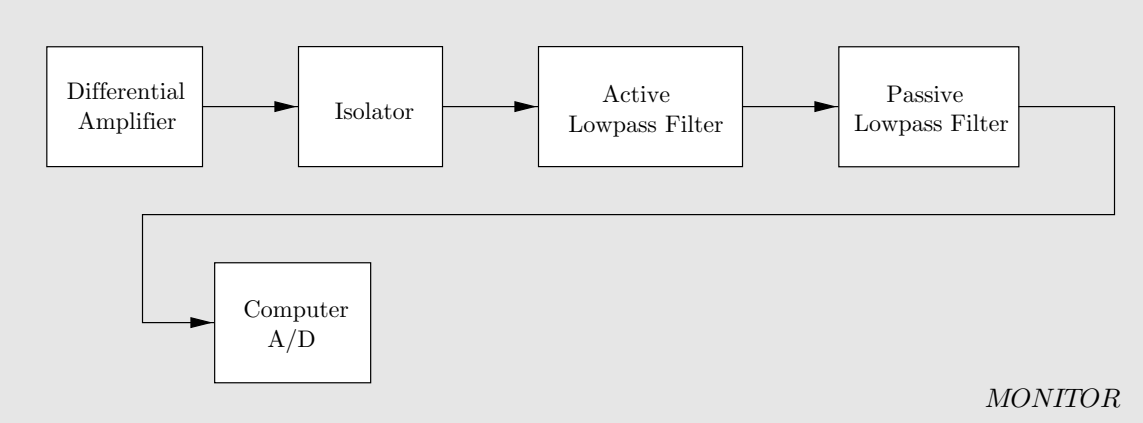

Figure B.8: Block diagram of one stimulus monitor.

circuit consists of a differential amplifier, an isolation network identical to that used in the stimulator circuit, an active lowpass filter, and a passive lowpass filter.

B.3.1 Differential amplifier

A schematic diagram of the differential amplifier at the stimulus monitor input is shown in Figure B.9. Op-amps TCL274A and TLC274B provide a differential gain of $[2(R_A/R_B) + 1]$. For measuring current I used $R_A = 23.7\text{k}\Omega$ and $R_B = 2.49\text{k}\Omega$ yielding a gain of 20.04; for measuring voltage I short-circuited R_A and open-circuited R_B for a gain of 1. Op-amp TLC274C converts the differential signal to single-ended with a gain of 1. A jumper, labeled "÷N", provided attenuation of monitor signals to avoid saturating the subsequent isolator circuit. For measuring current I set N=10 to provide optional 1/10 attenuation; For measuring voltage I set N=20 and always shorted the jumper terminals.

The TLC274 op-amps have high impedance MOSFET inputs, and were used to minimize the the amount of current shunted away from the stimulating electrodes by the monitor amplifiers. The three op-amp differential amplifier topology was chosen for its ability to completely reject common-mode steps at its inputs.

No special precautions were taken to minimize the offset voltages of the monitor amplifiers. The input offset voltages for the TLC274 op-amps can be as high as 10mV. In a worst case scenario, this would lead to a differential input offset voltage of 20mV, which in turn would yield 4V at the output of the current monitor. Luckily, the measured offset voltages are much smaller (see below). Perhaps we can assume from this that the input offset voltages of the op-amps within the TLC274 quad package are fairly well matched. In any event, the offsets are tolerable, so the design

DIFFERENTIAL AMPLIFIER

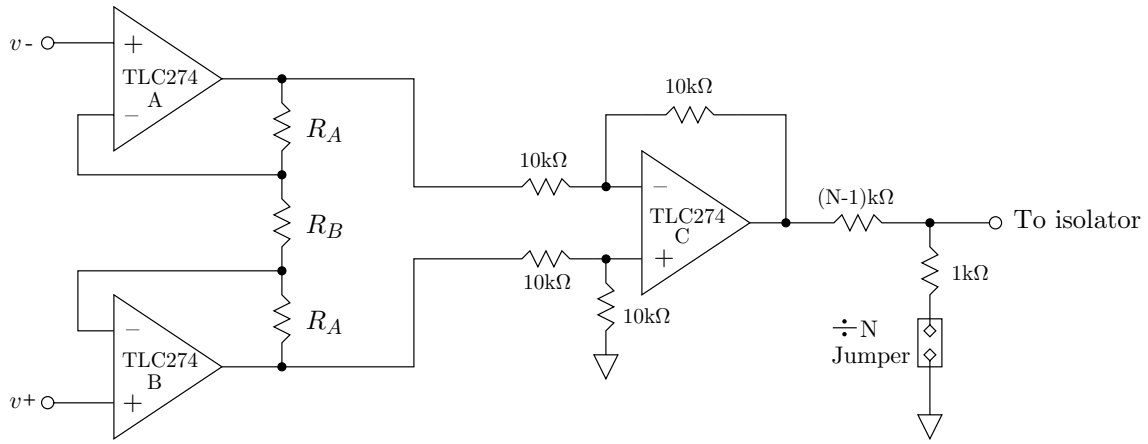

Figure B.9: Schematic diagram of the differential amplifier at the input of the stimulus monitor.

will be accepted as it is.

B.3.2 Isolation and filters

An isolation circuit, identical to that shown in Figure B.3 was used to isolate the differential amplifier ground (which is the same as the ground used for the voltage-controlled current source) from the computer A/D ground.

All of the comments made with regard to the use of the HCPL-7820 isolation amplifier in section B.2.1 are applicable here as well. The isolation amplifier is preceded by a buffer/drive and followed by 4 poles of lowpass filtering. The first of these poles is provided by the differential to single-ended converter (Figure B.3), the second and third poles by a Bessel filter (Figure B.4), and the fourth pole by a passive RC filter.

B.3.3 Performance Specifications

Monitor	÷N Jumper	Output/Input Ratio[1]	Output Offset[2]	Maximum Input[3]	10% - 90% Rise Time
1	ON	-.5 V/V	+12 mV	4 V	5 μs
2	ON	.2 V/μA	0 mV	10 μA	6 μs
2	OFF	2 V/μA	-110 mV	1 μA	6 μs

Notes:

1. The output to input ratio is set by a jumper labeled ÷N, where N=10 or N=20, on the circuit board holding the monitors.

   The ratio is calculated by taking the product of the measurement resistance (10kΩ), the differential gain (20), the attenuation (1/N), the isolator gain (8), and the Bessel filter gain (1.267).

2. The output offset voltage was measured with the monitor input terminals grounded.

3. The maximum input current is determined primarily by the limitation on the magnitude of the input to the HCPL-7820.

4. The monitors were driven with common mode steps of a few hundred mV, and no sign of these was observed on the outputs.

B.4 Nerve response amplifier design

In order to record from a large number of sites while maintaining reasonable hardware complexity, I built 8 amplifiers which can be electronically switched between each of 8 electrodes. This situation is depicted schematically in Figure B.10. To simplify the description of this design, a block diagram is shown in Figure B.11. The response amplifier circuit consists of several subcircuits. These include a multiplexer which connects one of 8 electrodes to the input of the amplifier cascade, a gain 10 preamplifier, an sample and hold circuit (to reduce stimulus artifacts), a two-pole active lowpass filter, and a high-gain amplifier.

B.4.1 Multiplexer

A schematic diagram of the multiplexer circuit for one amplifier channel is shown in Figure B.12. This circuit connects the preamplifier input to eight electrodes in parallel through electro-mechanical reed relays An analog multiplexer (ADG408) controls the flow of coil current such that only one relay is in the closed position at

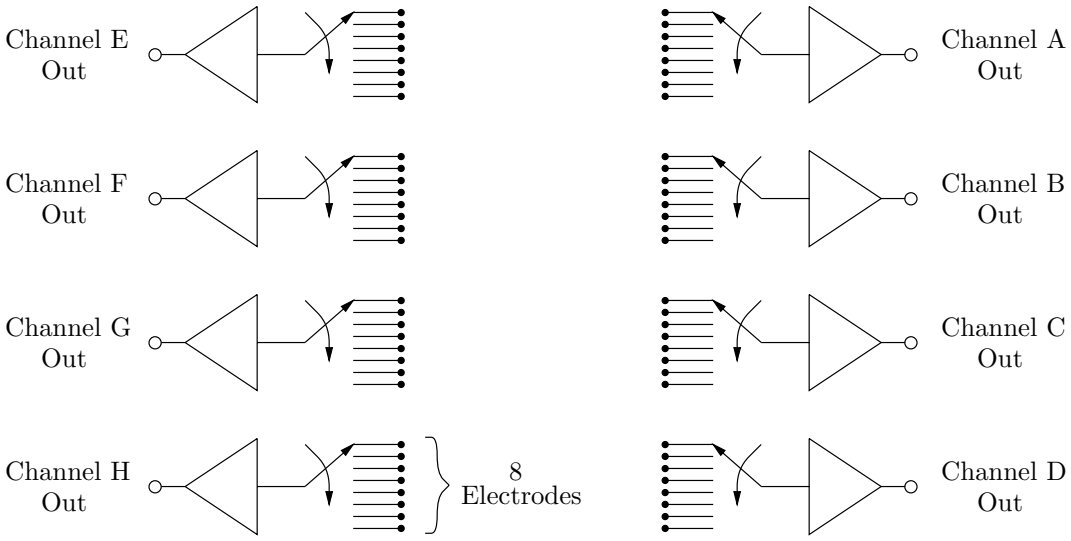

Figure B.10: Eight-channel nerve response recording system.

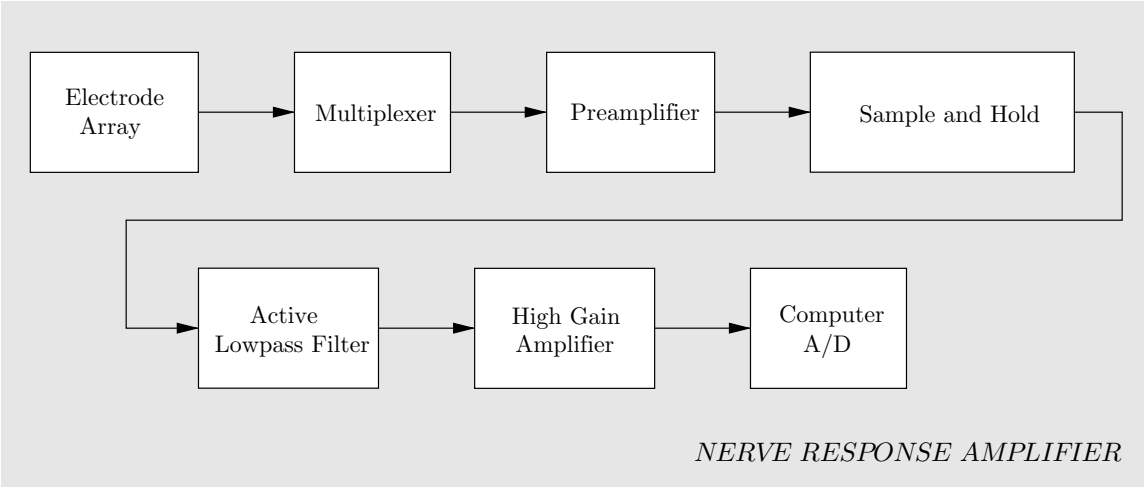

Figure B.11: Block diagram of one nerve response amplifier.

MULTIPLEXER

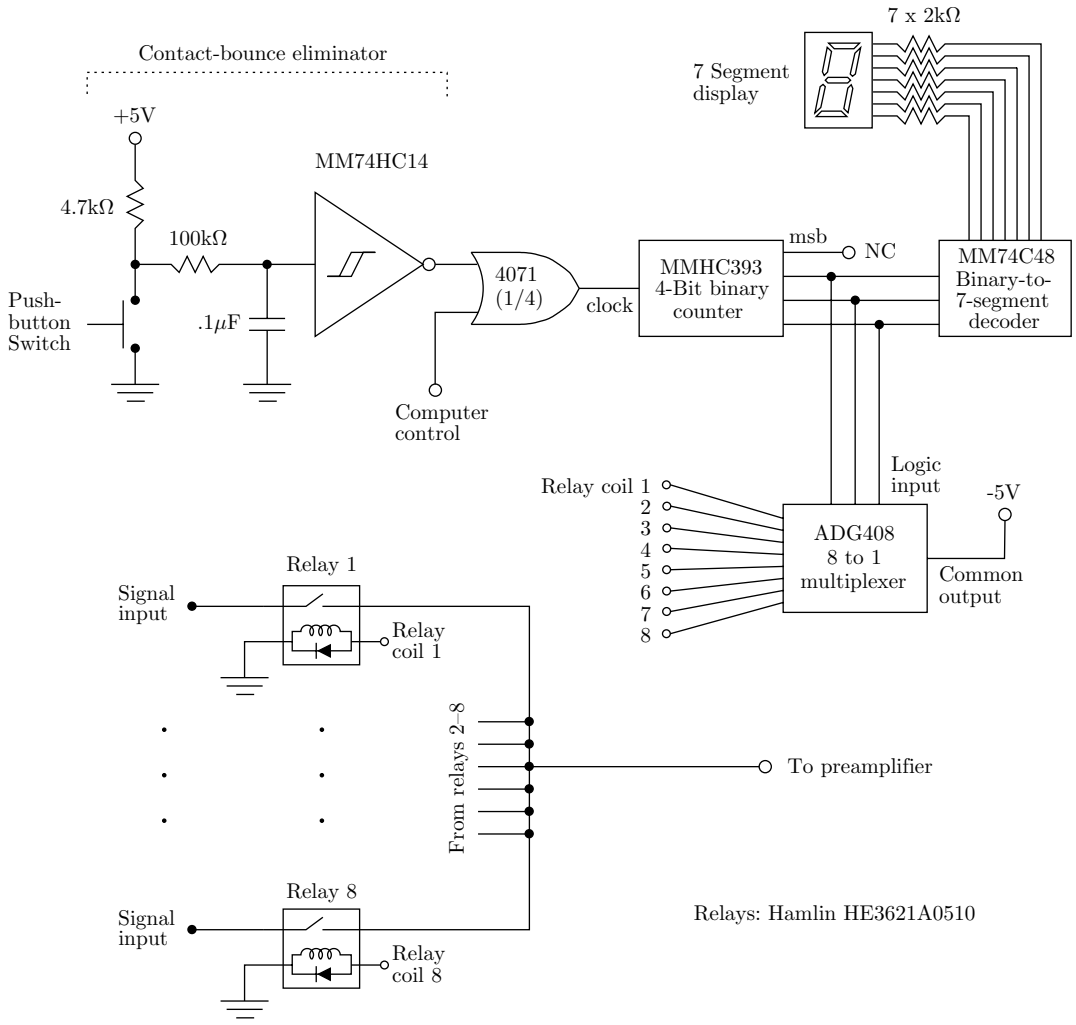

Figure B.12: Schematic diagram of multiplexer circuit for electrode selection.

PREAMP

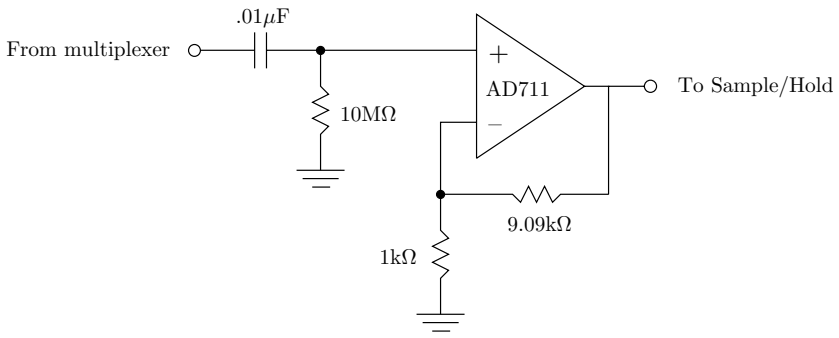

Figure B.13: Schematic diagram of the preamplifier circuit.

a time. The experimenter advances the multiplexer state to select a new electrode using a pushbutton on the front of the instrument panel. The state of the multiplexer is displayed as a digit between zero and seven with a seven-segment LED located on the front of the instrument panel. In addition, the multiplexers may be advanced under computer control.

B.4.2 Preamplifier

A schematic diagram of the preamplifier circuit is shown in Figure B.13. The multiplexer output is coupled to a standard non-inverting amplifier through a .01μF capacitor. This capacitor prevents the AD711 op-amp from drawing DC bias current through the electrodes. Instead, bias currents are provided by a 10MΩ resistor. The non-inverting amplifier provides a gain of (1 + 1kΩ/9.09kΩ) = 10.09. This provides a modest increase in signal level and a low-impedance driver for the long wires separating the preamplifier output (located near the retina) and the input of the sample and hold circuit (located in an instrument chassis a few feet away, in an equipment rack). The gain was kept small to reduce the likelihood of stimulation artifacts saturating the preamplifier.

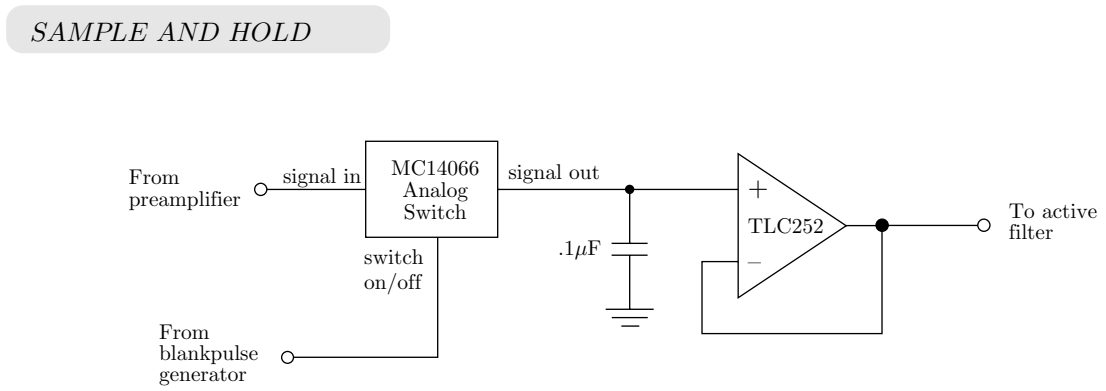

Figure B.14: Schematic diagram of the sample and hold circuit.

B.4.3 Sample and hold

A sample and hold circuit is placed between the preamplifier and the subsequent circuits in order to block transmission of artifacts during stimulus application. A schematic of the circuit is given in Figure B.14.

Normally the analog switch (MC14066), placed between the preamp output and a .1μF sampling capacitor, is closed. A logic pulse accompanying stimulation opens the switch for a brief interval. A special circuit shown in Figure B.15 generates a blanking pulse which starts before and ends after the current control waveform is coupled to the stimulator. This helps to ensure minimal coupling of the stimulus to the amplifier output.

The sampling capacitance was made as large as possible to minimize switch artifact (due to charge dump accompanying large voltage swings at the control input of the MC14066), but not so large that RC delays associated with the switch resistance could severely attenuate action potentials. The typical ON resistance of the MC14066 at room temperature is 120Ω (assuming 10V across the power rails). For C=.1μF, the 3dB cutoff frequency is 13.3kHz, which is about where we want it. The maximum ON resistance is 500Ω, which yields a somewhat low but tolerable 3dB cutoff of 3.2kHz. The measured resistance for the 4066 chip used for channels C and D is 88Ω (3dB cutoff at 18kHz).

The sampled voltage on the .1μF capacitor is buffered using a TLC252 MOSFET-input op-amp.

BLANKPULSE GENERATOR

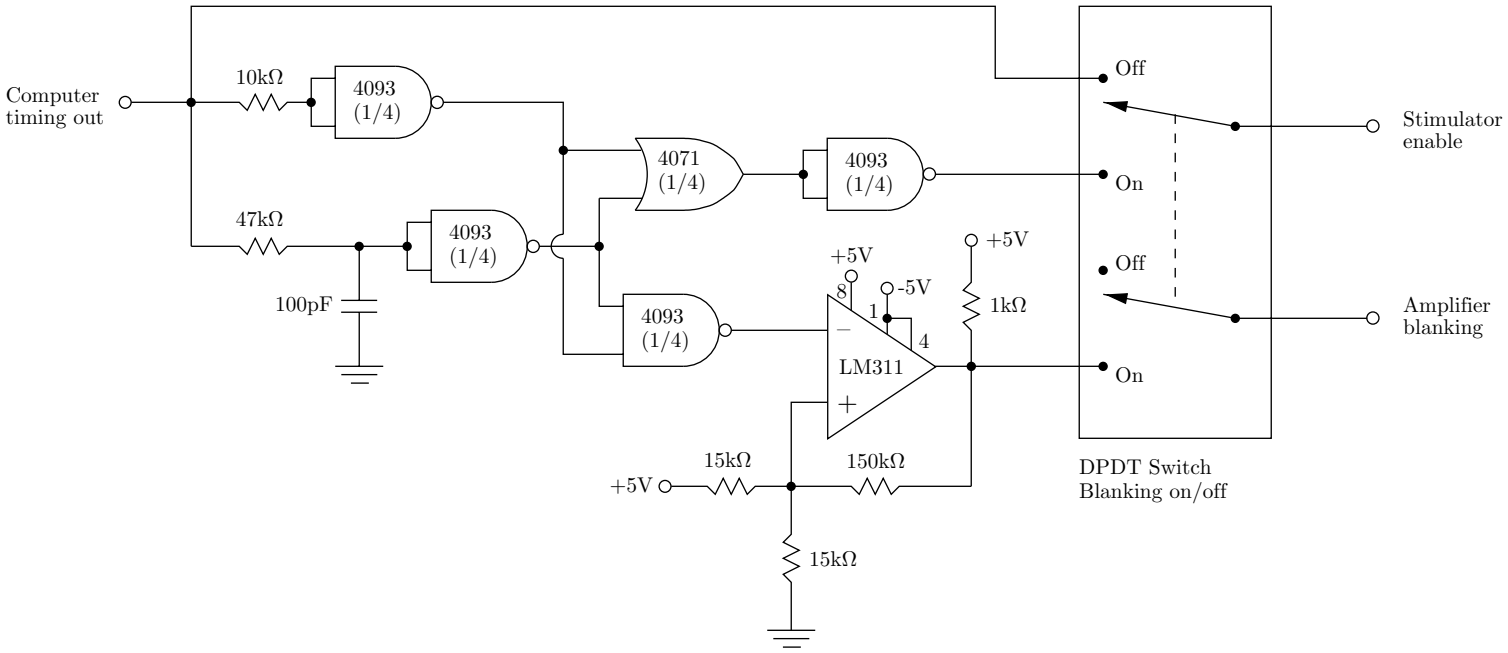

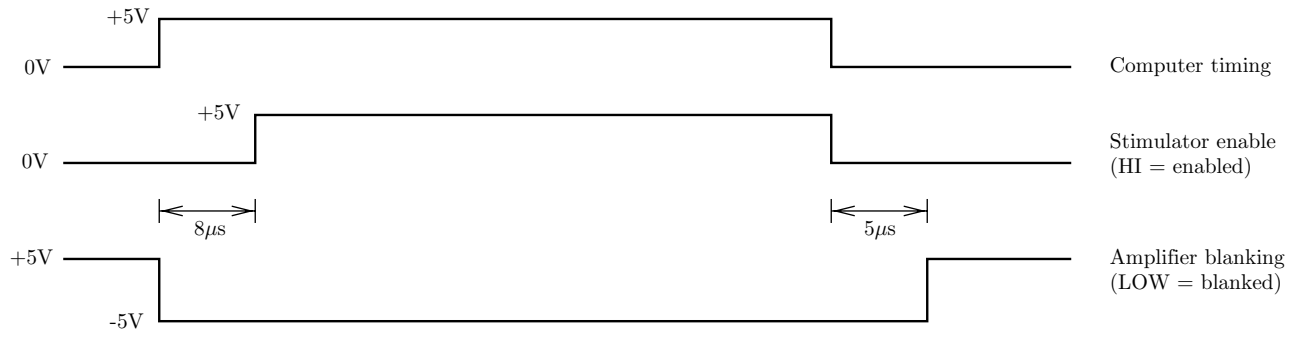

Figure B.15: Circuit for generating blanking pulses.

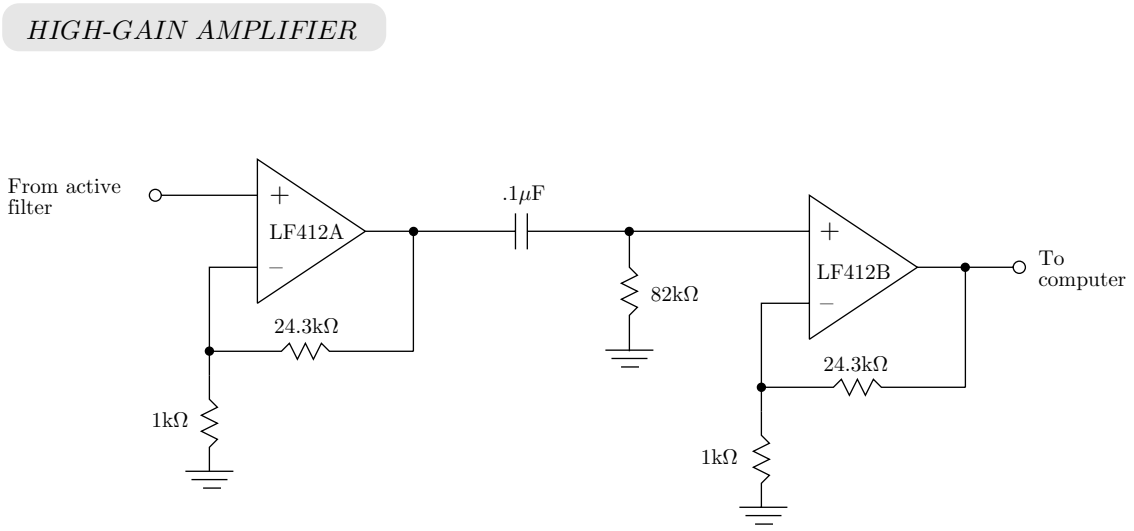

Figure B.16: Schematic diagram of the high gain amplifier.

B.4.4 Active lowpass filter

An active lowpass filter is used to reduce noise components which are outside of frequency ranges of interest. The filter is a second-order Butterworth type, and is used for its ability to provide a relatively sharp transition band while maintaining flat gain in the pass band. To implement the filter, the general active lowpass filter circuit of Figure B.4 is used with R_1=15.2kΩ, C_1=.001μF, R=100kΩ, and K=1.59. The calculated 3B-cutoff of the filter is 10.5kHz, and the low frequency gain is 1.59.

B.4.5 High-gain amplifier

Having been selected, preamplified, sampled and held, and filtered, the signal is finally fed to a high gain circuit. A schematic diagram of this circuit is shown in Figure B.16.

The gain of each of the non-inverting stages is (1 + 24.3kΩ/1kΩ) = 25.3. The passive high-pass filter formed by the .1μF and 82kΩ resistor placed between the two stages removes DC offset at the output of first non-inverting amplifier. The cutoff of the highpass is 19.4Hz, well below frequencies associated with extracellular action potentials.

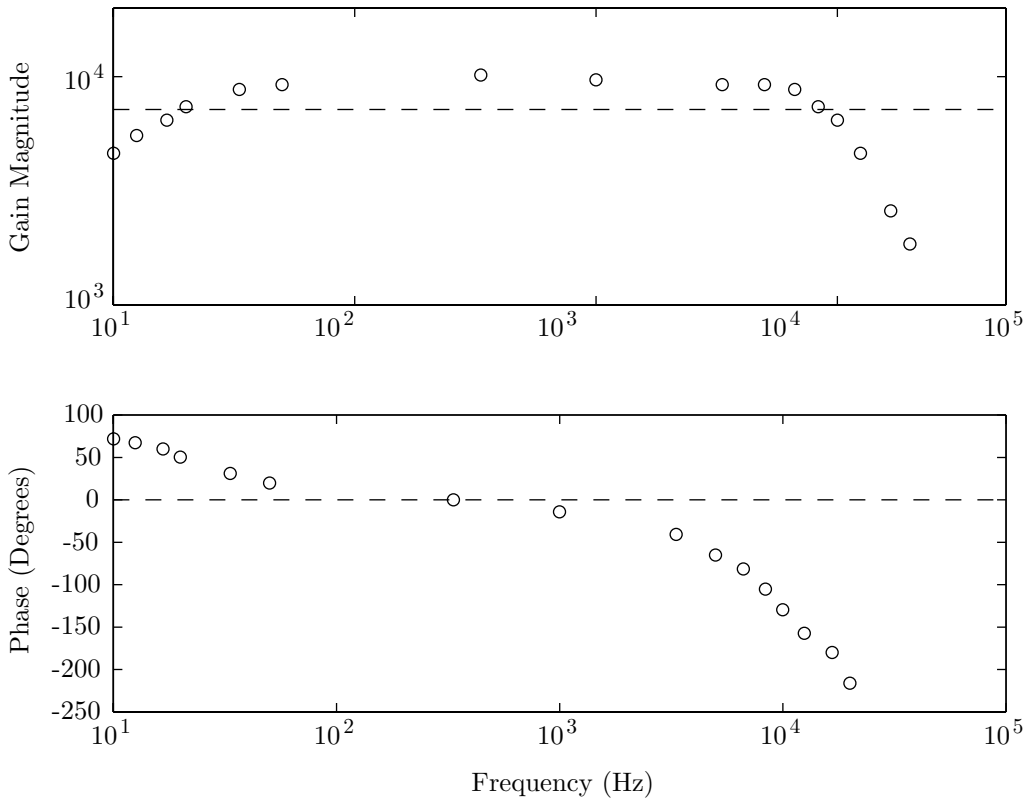

Figure B.17: Gain and phase plots for nerve response amplifier A. The dashed line in the gain plot is 3dB down from the midband gain.

B.4.6 Bode plot

A Bode plot of amplifier "A" is shown in Figure B.17. The measured gain of the amplifier is near 10,000, which is consistent with the calculated value of 10,177. This is found by taking the product of the preamplifier gain (10), the Butterworth filter gain (1.59), and the high-gain amplifier gain (25.3×25.3). The lower 3dB cutoff occurs near 20Hz, as predicted from the highpass cutoff of the passive RC in the high gain amplifier. The upper 3dB cutoff is at approximately 10kHz and the roll-off is steep, as we would expect from two poles in the active filter and the passive pole through the switch in the decoupler circuit.

B.5 System considerations

Three aspects of the circuits described above become most significant when the entire system is connected. These are noise, shunting of stimulator current, and stimulus artifacts. The first two topics are considered below, with another chapter devoted to the somewhat more involved third topic.

B.5.1 Noise

Ideally, when there is no cell activity, there will be no signal at the output of the nerve response amplifiers. In practice, this is not the case. Several sources may contribute noise at the output of the amplifiers, including pickup through the bath of noise generated by the stimulator, electrostatic pickup of noise generated by sources near the amplifier, ground loop pickup of noise generated by sources near the amplifier, and noise generated in the electronic components which are used to provide amplification.

Figure B.18 is a representation of the electronic instruments connected in a realistic configuration. The stimulator and nerve response amplifier are connected to electrodes in a salt water bath. The computer's analog output is connected to the stimulator, which is represented in the Figure as a voltage-controlled current source. The output of the nerve response amplifier is connected to an oscilloscope. Note that the nerve response amplifier and non-isolated side of the stimulator (to the left of the isolation barrier) are powered by different supplies than the isolated side of the stimulator (right side of the isolation barrier). Each set of supplies has its own common, or ground, node: the non-isolated ground is called "com1" in Figure B.18 and the isolated ground is called "com2". Note also that the wired connection labeled $\boxed{1}$ is made, so that "com1" is the same as "earth"[‡] The significance of labeled branches $\boxed{2}$ and $\boxed{3}$ will be considered below in the sections on electrostatic and ground loop pickup. Branch $\boxed{3}$ is shown as a dashed line because it is normally open-circuited.

With the configuration of Figure B.18 and no retina in the salt water, a measurement of the noise was made, sampling every 2μs for 10,000 counts. After subtracting off the absolute value (due to offsets in the amplifier cascade), the output noise amplitude is 52mV rms.

Stimulator-generated noise

Recall from section B.2.3 that the output of the HCPL-7820 isolator is somewhat noisy, and that an electronic switch was added to decouple the isolator from the bath during periods when the stimulator is not in use. Closing the switch was sometimes found to increase the noise on a recording electrode by as much as a factor of ten,

[‡]As it turns out, the ground provided by the plug-in supply which provides power to the non-isolated side (Va and Vb in the Figure) is not equal to the earth potential, so this connection must be made explicitly in order to use a computer or oscilloscope to make single-ended measurements of the amplifier output.

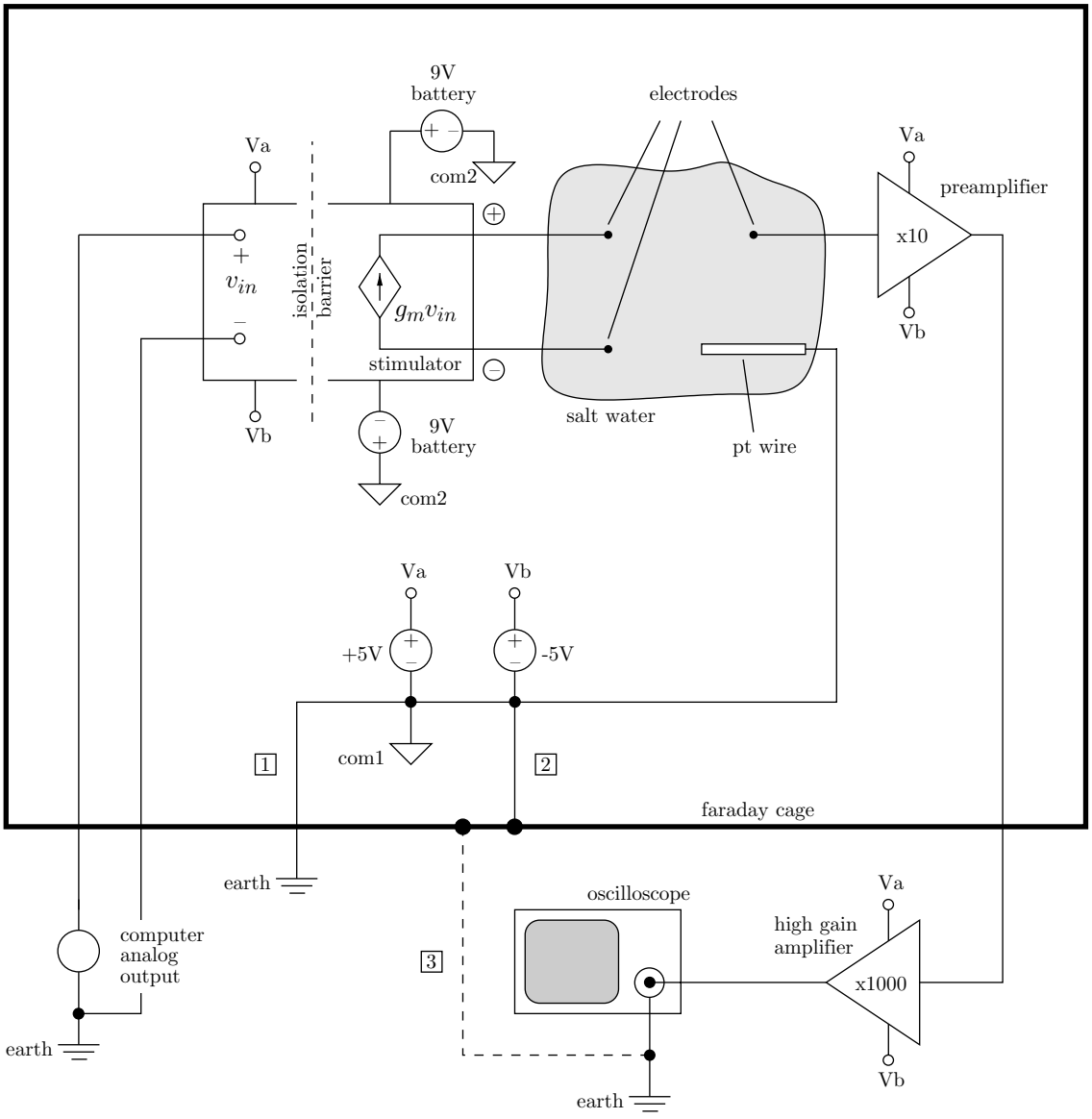

Figure B.18: Schematic diagram of the connected instruments. The current monitor amplifiers are not shown.

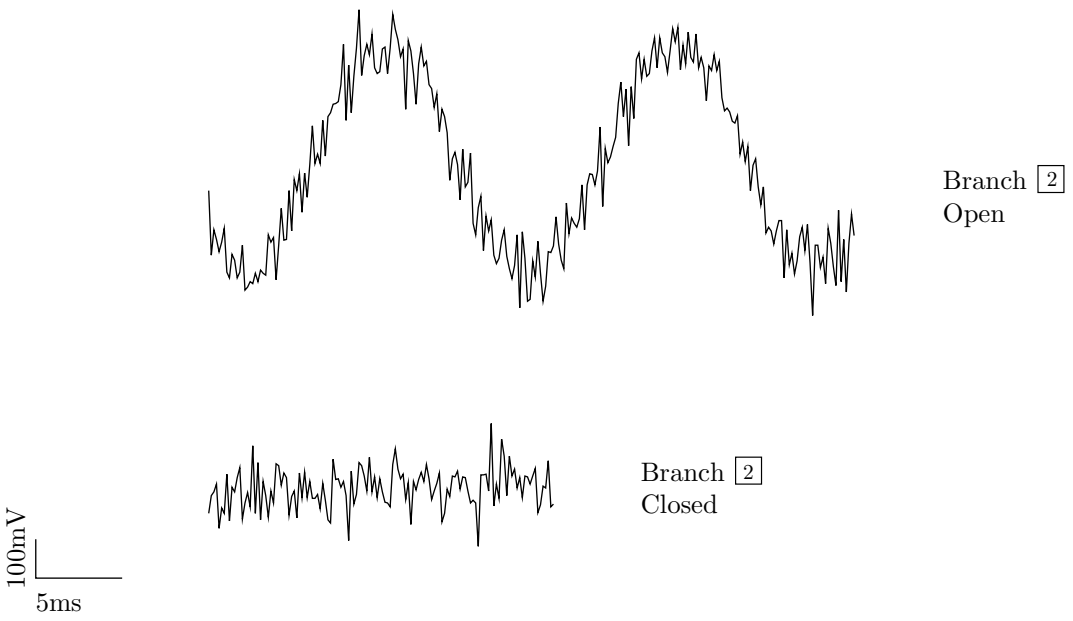

Figure B.19: Noise voltage measured at the amplifier output with branch 2 (Figure B.18) open and closed.

depending on the quality of insulation used and the relative positions of stimulating and recording electrodes. Thus for noise reduction it is advantageous to keep the switch open whenever the stimulator is not in use.

Electrostatic pickup

The input to the high gain amplifier has a very high impedance to ground, even when coupled to earth through the salt water bath. This makes the input node susceptible to capacitive coupling of noise sources in the environment. A Faraday cage, connected to the signal reference potential near the point of signal origination, should eliminate any capacitive coupling (Morrison, 1986). This notion can easily be checked by open-circuiting branch 2 (Figure B.18). Indeed, there is substantial pickup of 60Hz noise, as shown in Figure B.19.

Ground loop pickup

Noise can also be picked up via magnetic interactions when there are ground loops linking flux from a source near the amplifier. Closing branch 3 (Figure B.18), for example, generates such a loop. The path of the loop is illustrated in Figure B.20, which portrays a realistic layout of the ground connections initially used. The ground loop begins at the earth connection in the computer D/A, runs through the "common" node of the nerve response amplifier and through the Faraday cage, and then through the outer shell of the oscilloscope connector back to earth. Figure B.21 shows that under these conditions there is pickup of high frequency noise, which turns out to be near 30kHz. The total noise amplitude is not dramatically increased by the ground loop noise, though the root-mean-square magnitude rises from 52mV to 82mV.

This noise is apparently generated by the nearby computer monitor, since, even with branch 3 closed, the noise disappears when the computer monitor is turned off. With the monitor turned on and branch 3 closed, furthermore, the noise is reduced if physical wire constituting branch 3 is moved far from the monitor. In any event, the magnetic pickup in this case is eliminated easily enough by open-circuiting branch 3.

Noise generated by electronic components in the amplifier cascade[§]

The electronic devices used to build the nerve response amplifiers will also contribute to noise at the output. Unlike the sources discussed above, these sources are intrinsic to the amplifier and essentially inescapable[¶].

Device noise can be estimated from the equivalent input voltage noise e_n ($V/\sqrt{Hz}$) of the source in question, the gain applied between the source and the amplifier output, and the bandwidth over which the gain is large. Table B.1 summarizes estimates for the dominant contributors of device noise. For each of the operational amplifiers, the equivalent input voltage noise at 1kHz, e_n, was taken from the data sheets and assumed to be constant over the appropriate bandwidth.

We can make an estimate of the contribution of device noise if we assume that the noise sources in the Table are independent of one another. In this case the noise is the square root of the sum of the squares of the individual contributions. This value turns out to be 25.9mV rms, or roughly half of the measured value of 52mV rms. Thus, device noise, as estimated here, cannot be the dominant noise source.

As a check on our logic, note that we can connect the preamplifier input to earth without affecting the validity of our estimate for device noise. Under this condition,

[§]These measuresuments and calculations were performed during an earlier revision of the circuit in which the 3dB-bandwidth was 15kHz rather than 10kHz. Though the numbers would be slightly different for the present system, the main message of the section remains the same.

[¶]Of course, "low-noise" and "very low noise" circuit components are usually available. We will see, however, that the dominant noise source in the instrument is not the purchased components, but the electrode-electrolyte interface. This source will be discussed shortly.

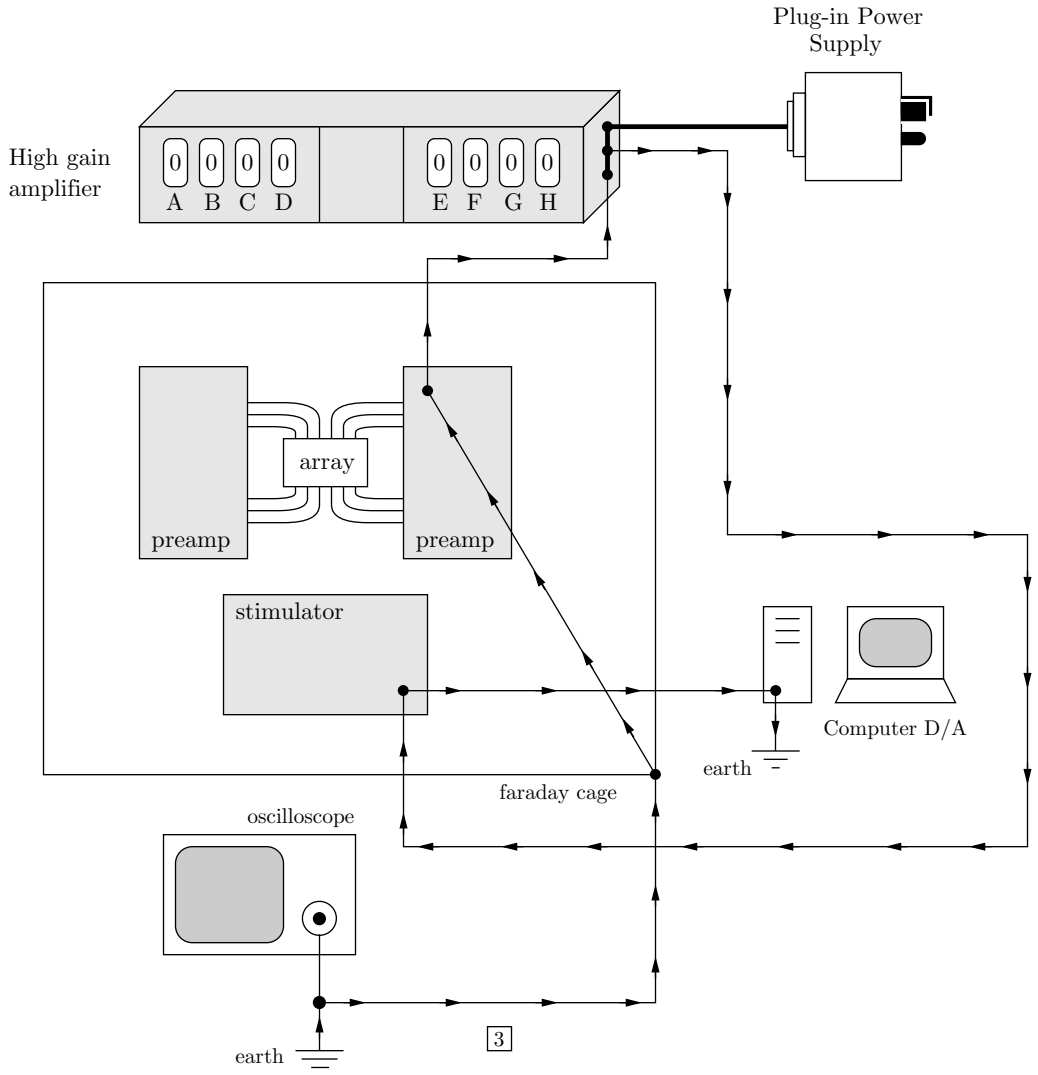

Figure B.20: Schematic diagram of ground connections leading to ground loop pickup from the computer monitor. Closing branch 3 between the oscilloscope BNC shell and the Faraday cage creates a ground loop (arrows) which links magnetic flux generated by the computer monitor.

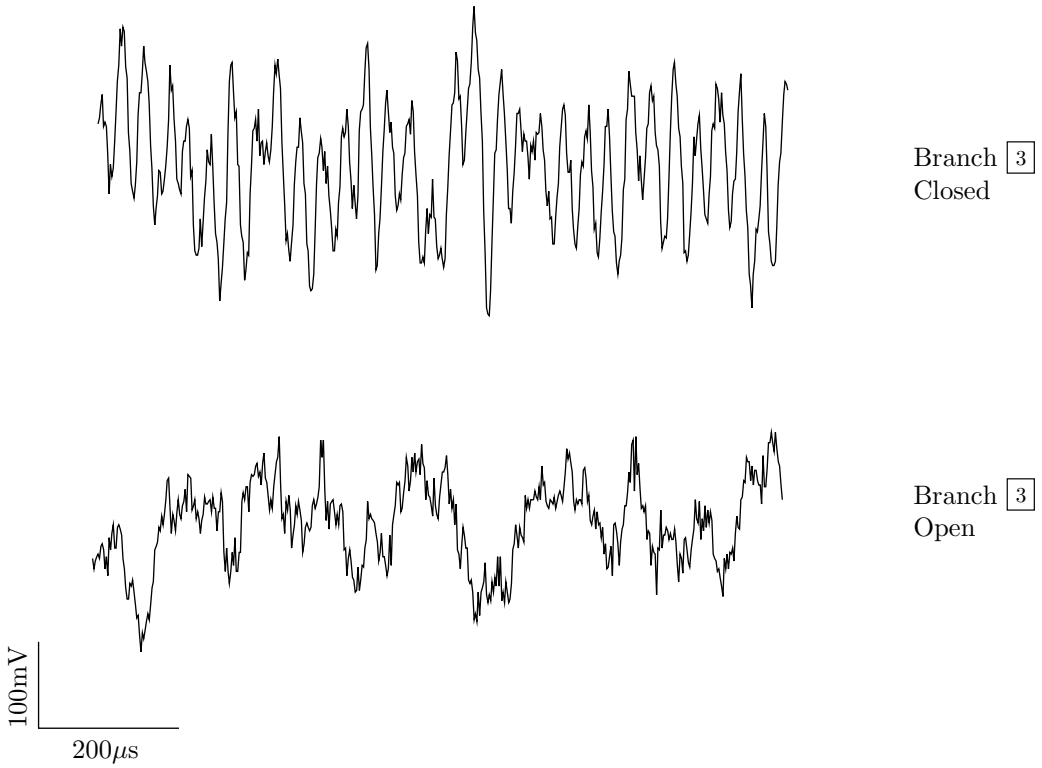

Figure B.21: Noise voltage measured at the amplifier output with branch 3 open and closed.

Source	Circuit Element	e_n (nV/$\sqrt{\text{Hz}}$)	$\sqrt{\text{Hz}}$	Gain	Output Noise at Voltage (mV rms)
1	AD711JN (Figure B.13)	18	$\sqrt{15\times10^3}$	10000	22
2	LF411 (Figure B.4)	30	$\sqrt{4\times10^6/25.3}$	1000	12
3	LF412A (Figure B.16)	25	$\sqrt{4\times10^6/25.3}$	640	6.4

Table B.1: Estimated contributions from major sources of noise in amplifier cascade.

the noise at the amplifier output is reduced to 31mV rms. This value is in reasonable agreement with our estimate of device noise.

Noise generated at the electrode-electrolyte interface

Electronic devices in the amplifier cascade generate a significant, but not dominant, fraction of the total observed noise. Some other source must therefore be responsible for most of the noise. Assuming this source is independent of those associated with the op-amps, its magnitude (integrated over the bandwidth of and multiplied by the gain of the amplifier) should be 41.7mV rms.

It seems most likely that the source of this noise is the electrode-electrolyte interface, since this component is eliminated when the interface is shorted out by earthing the preamp input terminal. A circuit model of the preamplifier input section is shown in Figure B.22. If we model the interfacial impedance Z_E as a resistor generating primarily Johnson noise, we would need $Z_E = 71\text{k}\Omega$ to generate the requisite 41.7mV rms. Measurements of the electrode impedance (see Figure B.23) reveal a complex impedance whose magnitude is in this range, but which has nonzero phase.

Further exploration of the interface noise might elucidate its mechanism, and possibly suggests ways to reduce it. At this point, however, it is worth noting that the total noise, referred to input, is about 5μV rms. In contrast, extracellular spike amplitudes are often 100μV or more, twenty times larger than the noise. Since the expected signal-to-noise ratio is quite good, the subject of noise will not be pursued further.

B.5.2 Current shunting

In Chapter 3 the field distribution in the tissue was controlled through a choice of stimulator connections to the electrode array. Even though the exact field distribution

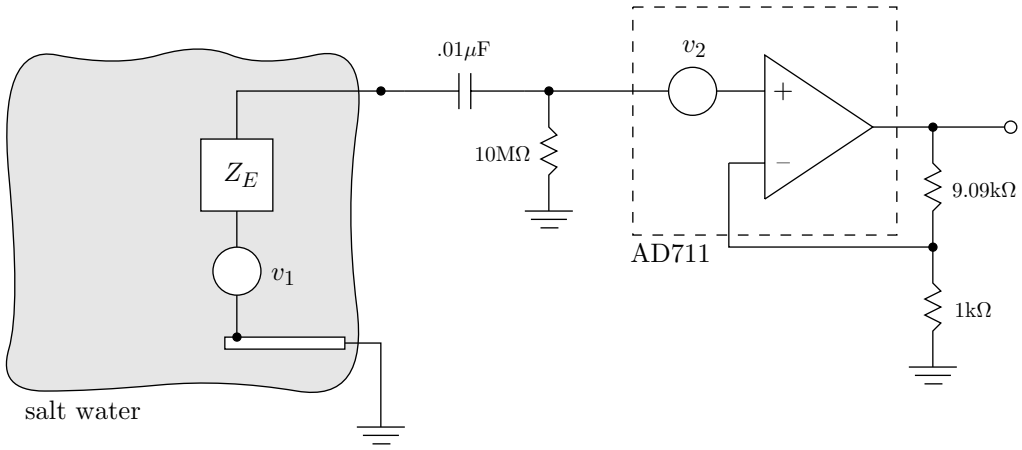

Figure B.22: Circuit model of the input region of the preamplifier. The interface impedance is Z_E, and the associated noise source has magnitude v_1. The equivalent input noise of the AD711 is in series with the + input terminal of the op-amp, and has magnitude v_2.

was unknown, a rough sense was obtained by assuming that current flowed only between the two conductors connected to the stimulator, and that the only available path was through the tissue. Initial instrument designs revealed conditions under which substantial shunt paths were available, weakening the above assumption. This section describes the nature of these paths and steps that were taken to reduce the amount of current flowing through them.

A generalized schematic of the instruments and possible shunt paths is shown in Figure B.24. For present purposes the nerve response amplifiers can be lumped together in a single box and only the output op-amp of the stimulator need be considered. The stimulator is connected between two electrodes, labeled p and n, through which currents i_+ and i_- flow. Three possible current paths, each a bold line ending in an arrow point, are depicted in the Figure. The box labeled Z represents pathways linking a node or nodes in the response amplifiers with the stimulator ground. The path labeled i_n passes through just the salt water (and tissue, if present) and represents the nominal or intended path for current flow. Hence in the ideal case $i_+ = i_- = i_n$.

The other two current paths, i_{sc} and i_{sd} are shunt paths. Let's consider first how current might flow in the i_{sc} path. Recall that if the stimulator op-amp is not saturated or slewing, the feedback requires that $i_- = -v_{in}/R_t$ and that electrode n is

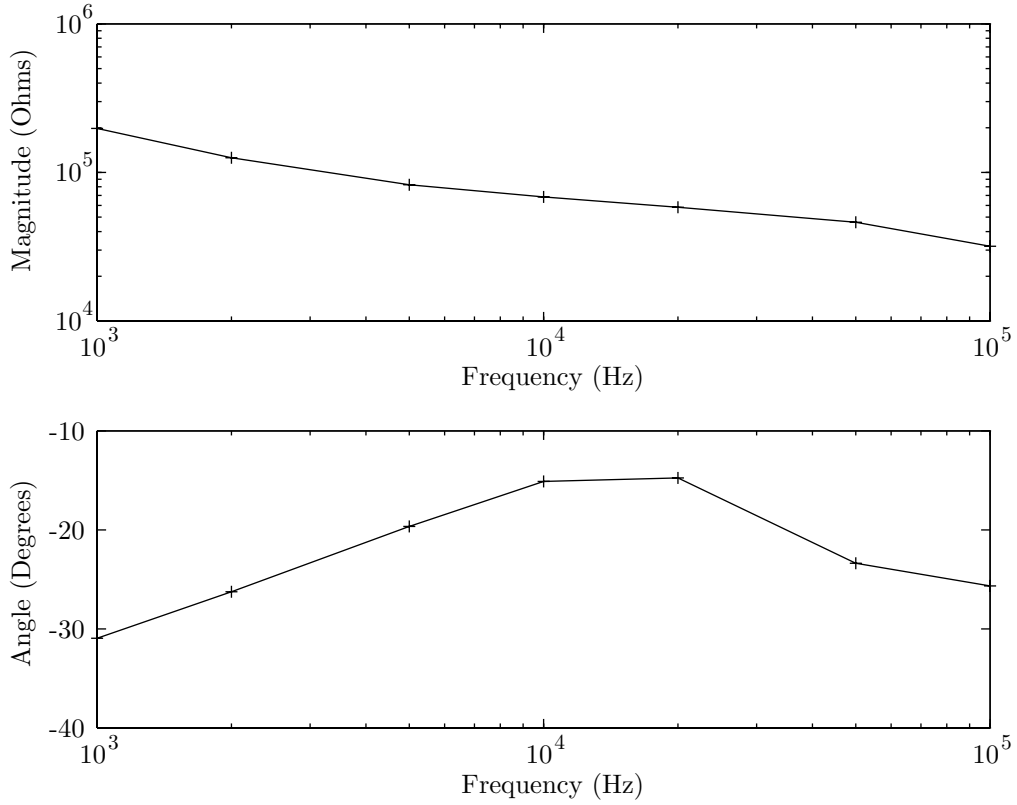

Figure B.23: Impedance magnitude and phase of electrode D0 on array AEG2. Electrode D0 is a 10μm diameter disk of indium-tin-oxide plated with platinum black at .3μA for about five seconds.

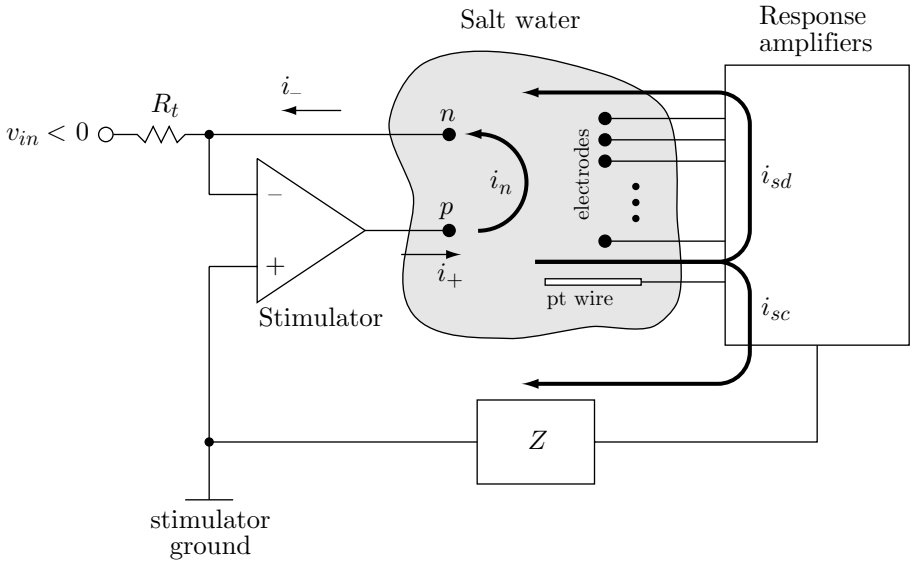

Figure B.24: Possible paths for stimulation current. i_n is the intended path; i_{sc} and i_{sd} are shunt paths.

at the stimulator ground potential. When $v_{in} < 0$, i_- and i_+ will be positive, raising the potential everywhere in the bath (relative to the stimulator ground) except at electrode n. This rise in potential may cause a current i_{sc} to flow if a sufficiently low impedance path between the amplifier and stimulator ground is available. The simplest such case would occur if the stimulator and recording amplifiers shared the same ground and if the recording amplifiers were configured for single-ended measurements. In this case the platinum wire would provide a direct connection to the stimulator ground.

In anticipation this outcome, the response amplifiers were initially configured for differential recording, with the platinum wire—which served as a common reference for all electrodes—connected to a high impedance op-amp input. Substantial shunt currents in the i_{sc} path were discovered in spite of this precaution. These were revealed when simultaneous measurements of the stimulator branch currents showed a transient period where $i_+ > i_-$. In this early version of the instrument, the stimulator and recording amplifiers shared the same ground, and analog multiplexers were used to select amplifier inputs as shown in Figure B.25a. The channel capacitances in the analog multiplexers provided low impedance paths to ground. All 64 such capacitances (8 multiplexers $\times$ 8 channels each) in parallel resulted in a significant shunt current, which appeared as an overshoot in the i_+ waveform. Consistent with this model, the overshoot systematically decreased as multiplexers were each replaced by

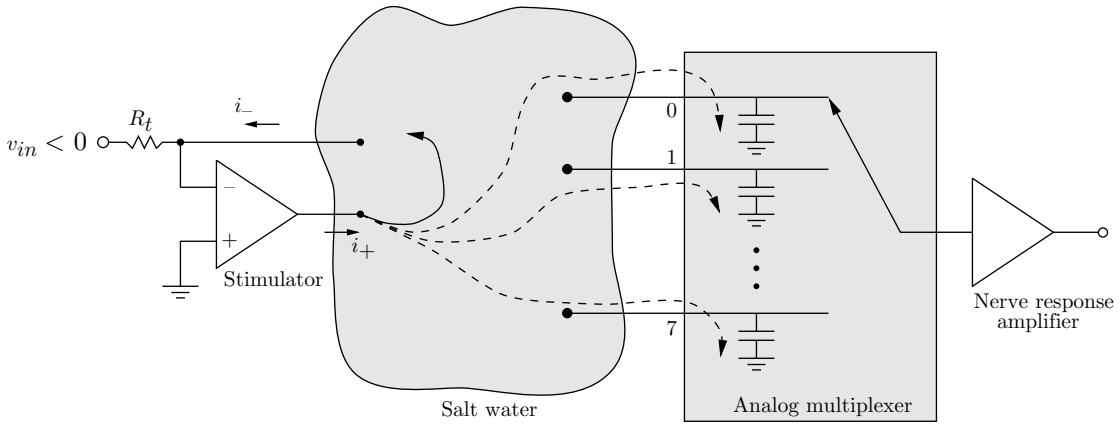

(a)

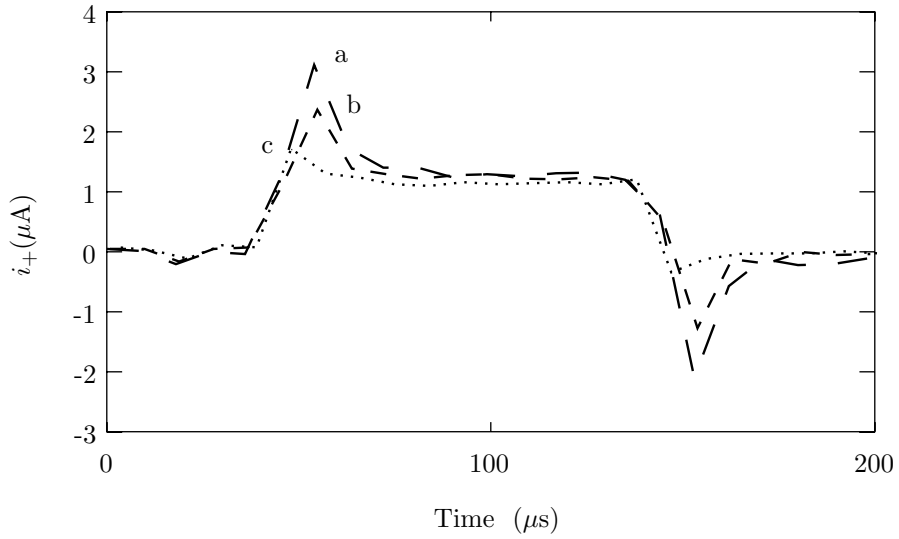

(b)

Figure B.25: Shunt currents with differential recording but a shared ground. (a) Schematic diagram of the instruments. The solid line represents the intended stimulation current, the dashed line is the shunt current. The capacitors represent parasitic channel capacitances to ground in the analog multiplexer. (b) Plot illustrating the dependence of the measured i_+ current on the number of multiplexers connected to the bath. The peak overshoots for three cases are labeled: a - four multiplexers; b - 2 multiplexers; c - no multiplexers.

a wired connection from one electrode to the preamplifier input. This is shown in Figure B.25b.

Isolating the stimulator from the response amplifiers, so that the two use separate grounds, reduces if not abolishes the i_{sc} component. Even with all eight multiplexers connected, the measured i_- and i_+ current components were equal. This approach required that care be taken to keep the two grounds physically separate to reduce parasitic capacitance between them. In the physical arrangement of the circuits, the stimulator was placed atop an insulating platform, several centimeters above the recording ground plane.

The second path for shunt current, labeled i_{sd} in Figure B.24, is more subtle. This path is taken by current which flows into the response amplifier through some electrodes and back out through others. The shunting cannot be detected from measurements of the stimulator branch currents since isolation ensures that the branch currents are equal. However, the relatively large channel capacitances in the analog multiplexer might be expected to provide viable paths as they did in Figure B.25, but instead joining different electrodes via the recording ground. The electro-mechanical relays in Figure B.12 were introduced for this reason. The parasitic capacitances to ground associated with these were measured at 1-2pF, as opposed to several tens of pF for the analog multiplexers.

B.5.3 Summary of ground connections

The observations of Section B.5.1 suggest using the ground connection scheme illustrated in Figure B.26. To eliminate electrostatic pickup, the Faraday cage is connected to the shield around the power supply wires, which is in turn connected to earth. As mentioned at the beginning of section B.5.1, the power supply ground "com1" is connected to earth. To minimize the potential for ground loop pickup, the earth-connections from the computer D/A and plug-in power supply will be kept in close proximity to one another, as shown in the Figure. Finally, a branched ground connection is used, wherein all grounds are established at a central "hub".

B.6 Dynamic response of current source output network

The stimulator current source and output network are redrawn in Figure B.27, with the op-amp circuit replaced with an ideal current source. To simplify analysis, the electrodes have been modeled with a resistor R_L.

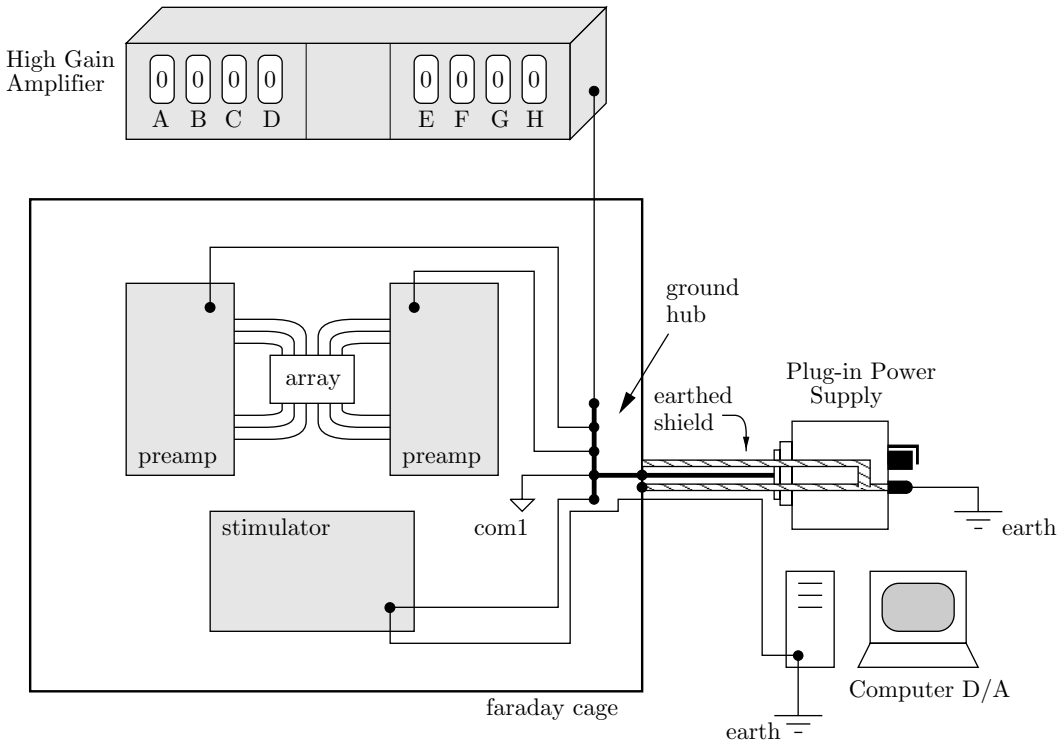

Figure B.26: The ground connection scheme used.

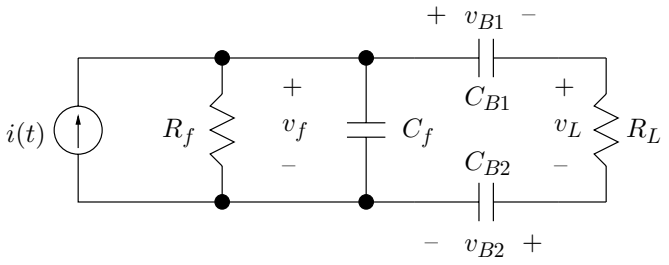

Figure B.27: Ideal current source and output network.

B.6.1 Derivation of transfer function and natural frequencies

Here are the fundamental circuit equations for the network:

$$i(t) = \frac{v_f}{R_f} + C_f \frac{dv_f}{dt} + C_B \frac{dv_{B1}}{dt},$$

$$\frac{v_L}{R_L} = C_B \frac{dv_{B1}}{dt} = C_B \frac{dv_{B2}}{dt},$$

$$v_f = v_L + v_{B1} + v_{B2}.$$

Taking the derivative of the first equation and solving the system for d_i/dt yields

$$\frac{di}{dt} = (C_f)\,\frac{d^2 v_L}{dt^2} + \left(\frac{1}{R_L \| R_f} + \frac{2C_f}{R_L C_B}\right)\frac{dv_L}{dt} + \left(\frac{2}{R_f R_L C_B}\right) v_L.$$

Converting to the frequency domain, and noting that the load current i_L is the quotient of the load voltage v_L and load resistance R_L, we find that the transfer function from stimulation current to load current is

$$\frac{I_L(s)}{I(s)} = \frac{s/R_L C_f}{s^2 + \left(\frac{1/C_f}{R_L \| R_f} + \frac{2}{R_L C_B}\right) s + \frac{2}{R_f C_f R_L C_B}}$$

The natural frequencies of this circuit are the roots of the characteristic equation,

$$s^2 + \left(\frac{1/C_f}{R_L \| R_f} + \frac{2}{R_L C_B}\right) s + \frac{2}{R_f C_f R_L C_B} = 0.$$

These roots are

$$s = -\left[\frac{1/2}{(R_L \| R_f) C_f} + \frac{1}{R_L C_B}\right] \pm \sqrt{\left[\frac{1/2}{(R_L \| R_f) C_f} + \frac{1}{R_L C_B}\right]^2 - \frac{2}{R_f C_f R_L C_B}}.$$

The resistance R_L represents the series combination of two electrodes and the bath. This should be somewhere between 100 kΩ and 1 MΩ. The feedback resistor R_f is 10 MΩ. If we approximate $R_L \ll R_f$, the roots of the characteristic equation can be written

$$s \approx -\left(\frac{1/2}{R_L C_f} + \frac{1}{R_L C_B}\right)\left[1 \pm \sqrt{1 - \frac{2}{\left(\frac{R_f C_B}{R_L C_f}\right)\left(\frac{1}{2} + \frac{C_f}{C_B}\right)^2}}\right].$$

Noting further that C_f is 10pF and C_B is 10nF, we see that $C_f \ll C_B$. This being the case, the term under the radical in the expression above is very close to 1. Taking a first order approximation of the square root yields,

$$s \approx -\left(\frac{1/2}{R_L C_f} + \frac{1}{R_L C_B}\right)\left[2 - \frac{1}{\left(\frac{R_f C_B}{R_L C_f}\right)\left(\frac{1}{2} + \frac{C_f}{C_B}\right)^2}\right]$$

$$\text{OR} \quad -\left(\frac{1/2}{R_L C_f} + \frac{1}{R_L C_B}\right)\left[\frac{1}{\left(\frac{R_f C_B}{R_L C_f}\right)\left(\frac{1}{2} + \frac{C_f}{C_B}\right)^2}\right]$$

Finally, making use again of the approximations $R_L \ll R_f$ and $C_f \ll C_B$, we get

$$-\frac{1}{\tau_1} = s \approx -\frac{1}{R_L C_f} \qquad \text{OR} \quad -\frac{1}{\tau_2} = s \approx -\frac{2}{R_f C_B}$$

Fast Response Slow Response

B.6.2 Interpretation of circuit natural frequencies

The retina is stimulated using rectangular current pulses, so it is useful now to consider the step response of the load current. Rather than doing a full solution, a bit of circuit intuition will be used to predict the answer, and then comparisons with measurements made to check the reasoning.

Fast natural frequency

First, consider the "fast" response, where the dynamics are governed by the time constant $\tau_1 = R_L C_f$. On these time scales, the larger blocking capacitors C_B are essentially short circuits, and the current is used to charge up C_f. The (now) parallel combination of R_L and R_f is dominated by the smaller R_L, so the dynamics are essentially those of the simplified circuit of Figure B.28a. The step response of the current $i_L(t)$ is given by

$$i_L(t) = \mathrm{I}\left(1 - e^{-t/R_L C_f}\right)$$

This response is drawn in Figure B.28b. Part c of the Figure illustrates the relatively good agreement between predicted and measured responses for R_L=240kΩ and C_f=100pF.

Note that a larger capacitor C_f was used for this measurement than the normal value of 10pF (see Figure B.7). For C_f=10pF, the step response of the current does not resemble an exponential function, but instead exhibits a rapid rise time (less than half a microsecond) and a 20% overshoot. A second, and perhaps related, discrepancy is evident in the table of stimulator performance specifications given at the beginning of section B.2.5. Below the table, it is noted that the 10%-90% rise time was found to vary with the transconductance-setting resistor R_t. Neither the non-exponential step response nor the variation of rise time with R_t is predicted by the model of Figure B.27. This is most likely because for small feedback capacitances the operational amplifier circuit is not well-modeled by an ideal current source.

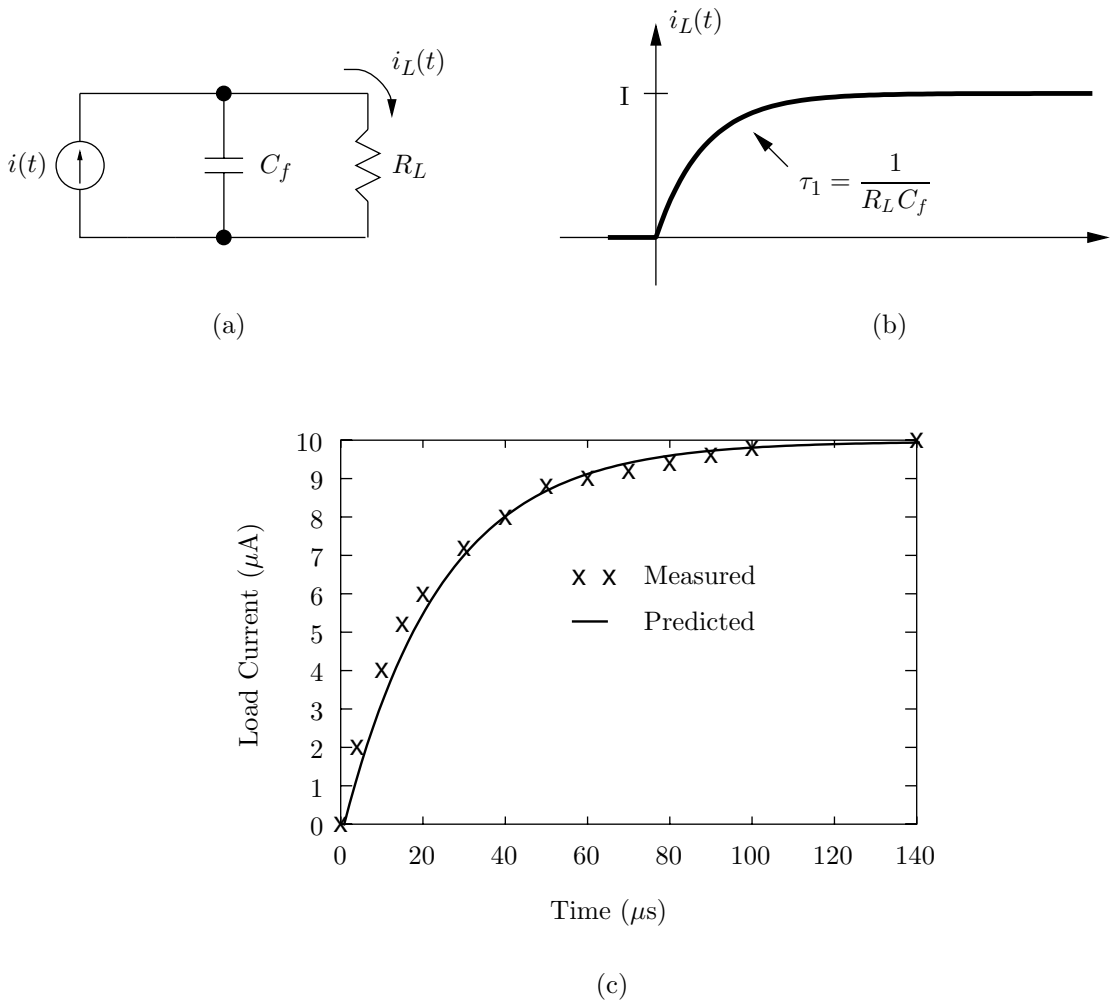

Figure B.28: Fast natural frequency: (a) circuit; (b) predicted step response; (c) and comparison of predicted and measured step responses.

Slow natural frequency

Now consider the "slow" response, where the dynamics are governed by the time constant $\tau_2 = \frac{1}{2}R_f C_B$. Looking at the circuit containing the ideal source and full output network, we recognize that, at DC, the load current must be zero since the blocking capacitors look like open circuits. We associate this second time constant with the slower discharging of the C_B's when the total charge delivered by a stimulation waveform is nonzero. In this case, C_f can be assumed to always be at its "final" voltage, since its dynamics are very fast on the time scale of interest here. We can therefore use a *quasistatic model* and treat C_f as an open circuit. Combining the two series C_B's, we redraw an approximate circuit in Figure B.29a.

The load current $i_L(t)$ is given by

$$i_L(t) = I_o e^{-t/\frac{1}{2}(R_f+R_L)C_B}$$

or, if we invoke the approximation $R_L \ll R_f$,

$$i_L(t) \approx I_o e^{-t/\frac{1}{2}R_f C_B}$$

where

$$I_o = \frac{2\mathrm{Q}}{(R_f + R_L)}$$

and Q denotes the amount of leftover charge delivered by the stimulus. This approximate response is shown in Figure B.29b.

Figure B.29c compares the measured (black) and predicted (superimposed white) responses of the load current when an unbalanced charge Q=9nF is delivered by a brief pulse of 10μA current. Again, the agreement between the theoretical and measured responses is satisfactory.

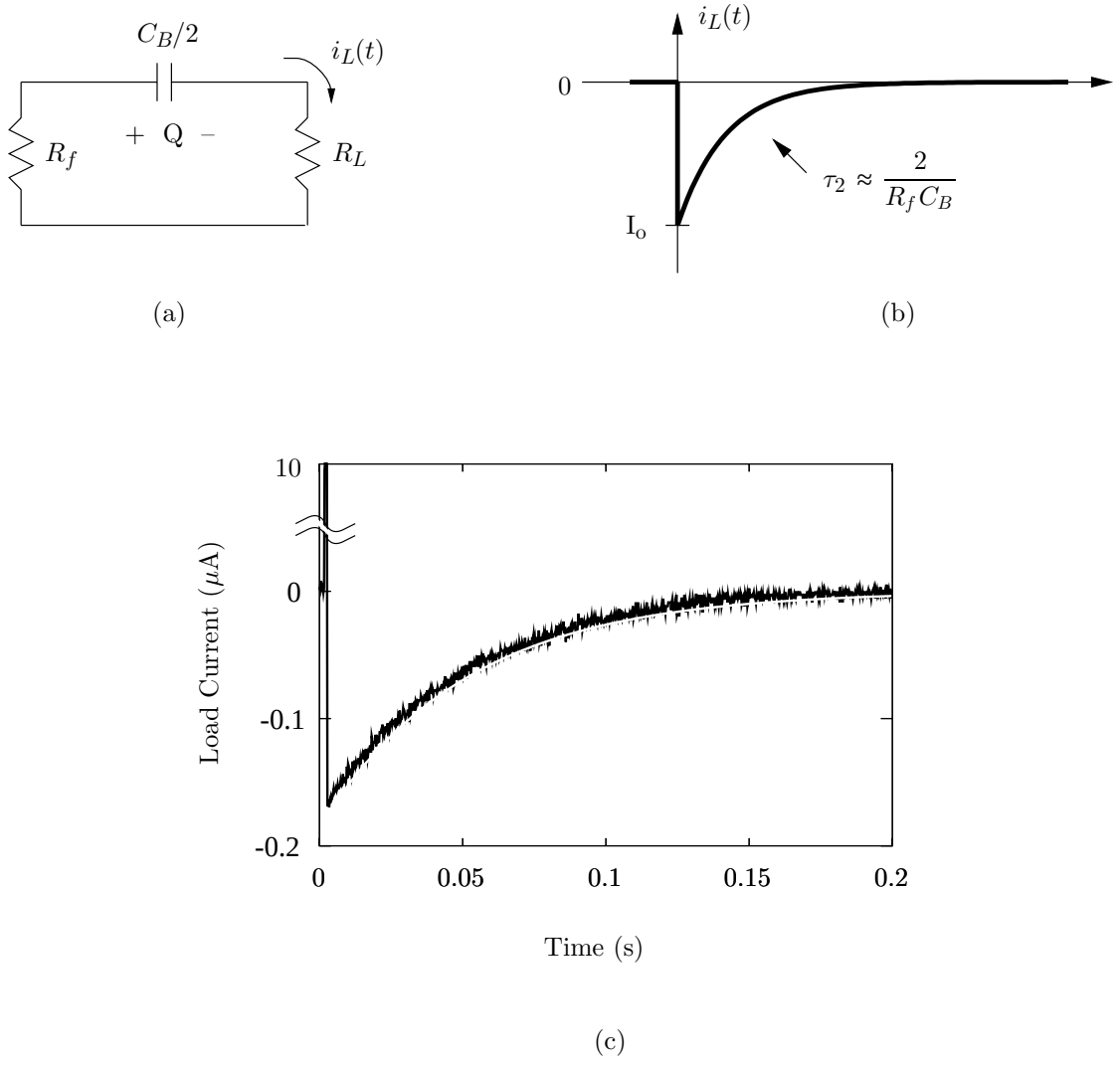

Figure B.29: Slow natural frequency: (a) approximate circuit; (b) step response; (c) comparison of predicted and measured step responses. In (c), the measured step response for R_L=240kΩ, $C_B = .01\mu$F is drawn in black and the predicted response is superimposed in white.

Appendix C

Investigations of Stimulus Artifact

C.1 Introduction

All experiments involving electric stimulation and recording suffer to some degree from stimulus-induced distortion of the response signal. The distortion is called the *stimulus artifact*, and is alternately referred to as the stimulus artefact or shock artifact.

Stimulus artifacts make it difficult if not impossible to study neural responses to electric stimulation. Consider for example Figure C.1, which depicts a recording that was taken early in the experimental work of this thesis. The artifact is large compared to a typical action potential, and substantially outlasts the stimulus. The artifact is large enough and long enough, in fact, that the amplifier is saturated during the interval where neural responses are expected to occur*. Thus no useful data can be obtained from this recording.

Stimulus artifacts can arise from any of a large number of sources. This chapter details efforts to identify these sources in the instrument system (see Chapter 2 and Appendix B) and to reduce their impact. An alternate approach, wherein signal processing is employed to discover response signals in artifact-contaminated recordings, was not pursued due to the not infrequent occurrence of amplifier saturation.

The material is presented in more or less the order in which the different approaches were tried. These efforts were not exhaustive, and many did not lead to a significant improvement in signal quality, but they did, along with a sampling of the relevant literature, help me to formulate a fairly broad view of the problem. This view is presented at the end of the chapter.

*Unlike light-generated ganglion cell responses (which lag the stimulus onset by tens to hundreds of milliseconds), electrically generated ganglion cell responses can be initiated within a millisecond.

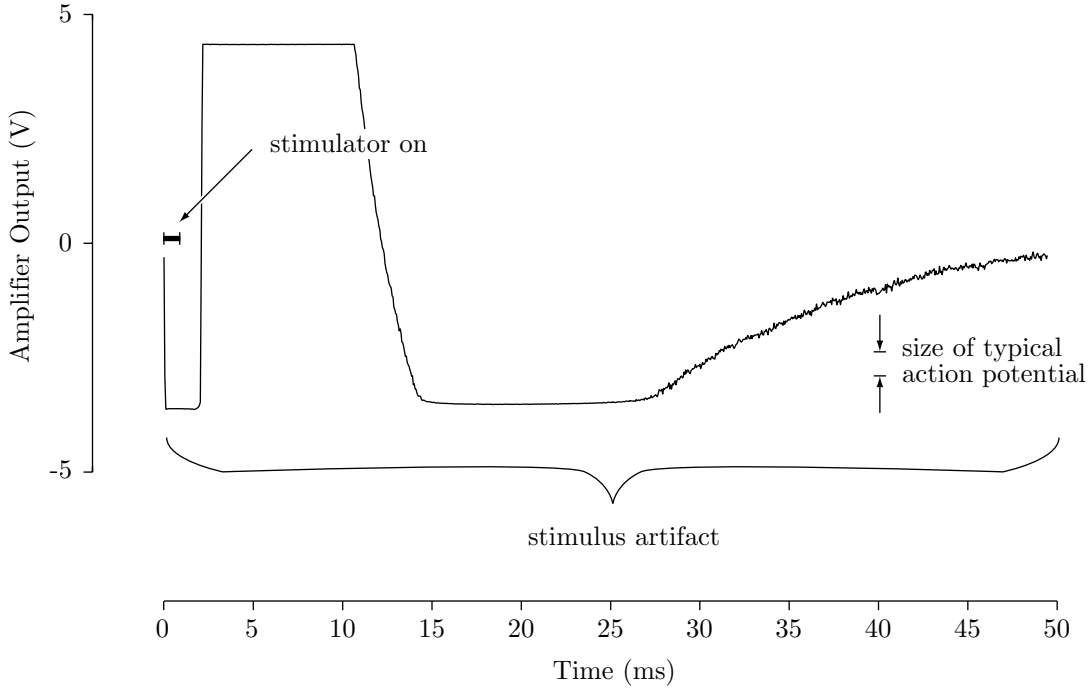

Figure C.1: Example stimulus artifact.

C.2 Response amplifier considerations

C.2.1 Saturation and filters

The potential changes produced at the response amplifier input by electric stimulation are often vastly larger than the expected response signal. These unusually large inputs drive the response amplifier into saturation, where the amplifier's behavior can be unpredictable. The suggestion arises that substantial length is added to the artifact by the amplifier circuit, as a result of being driven so far beyond its dynamic range (Freeman, 1971; McGill et al., 1982; Ranck, 1981; Sherman-Gold, 1993). The additional length might be attributed to erratic saturation behavior of individual op-amp chips or to slow discharging of high pass filter capacitors.

To see how high pass filters can add length to stimulus artifacts, consider the amplifier topology used for this thesis. A passive high-pass filter is placed prior to the final stage of x25.4 gain to block DC offsets from earlier stages, as shown in Figure B.16. Suppose now that a stimulus lasting 300μsec is applied, and that it is sufficient to saturate the input to the high-pass filter for the entire duration of

the stimulus. The saturation voltage driving the high-pass filter is roughly 5 volts (i.e. the positive supply rail). Since the time constant of the high-pass filter is much larger than than the interval of interest (8.2msec compared with 300μsec), the charge deposited on the capacitor will be approximately

$$Q = \frac{5\text{V}}{82\text{k}\Omega} \times 300\mu\text{sec} = 18.3\text{nC}.$$

If, when the stimulus is over, the output of the early gain stages returns immediately to zero, the charge on .1μF capacitor will result in a voltage

$$V = \frac{\text{Q}}{\text{C}} = \frac{18.3\text{nC}}{0.1\mu\text{F}} = 0.183\text{V}.$$

This voltage is sufficient to saturate the final gain stage, and decays with a very slow time constant of 8.2ms.

Note that the same principle could be applied to low-pass filters in the circuit, though in practice the time constants associated with such filters are usually fast enough to be of no consequence.

C.2.2 Sample and hold

Saturation problems and filter transients can sometimes be eliminated by inserting a sample and hold into the amplifier circuit (Freeman, 1971; Roby and Lettich, 1975; Sherman-Gold, 1993). Such a circuit is switched into "hold" mode just before stimulation, to store the baseline voltage and prevent large signals from being passed to later filters and stages of gain. When the stimulus is over, the circuit is switched back to "sample" mode, hopefully allowing the neural response signals to pass undistorted.

The amplifiers used in this thesis contain a sample and hold circuit, placed at the output of the x10 pre-amplifier (see Figure B.11 and Section B.4.3). Measurements such as that shown in Figure C.2 revealed that the artifact persisted even when the sample and hold circuit was used. Thus the artifact must have been present at the input to the sample and hold circuit, and cannot be attributed to filter transients or saturation of op-amps in the higher gain stages.

Incidentally, sample and hold circuits are sometimes employed even when the artifact ends promptly with the stimulus. The reason is that it eliminates transients from the signal which might be misinterpreted as physiologic signals by systems using automated event extraction schemes (Freeman, 1971; Minzly et al., 1993; Roby and Lettich, 1975).

C.2.3 Preamplifier input

The measurements above do not rule out the possibility that artifacts were generated in the pre-amplifier which precedes the sample and hold circuit. Direct examination

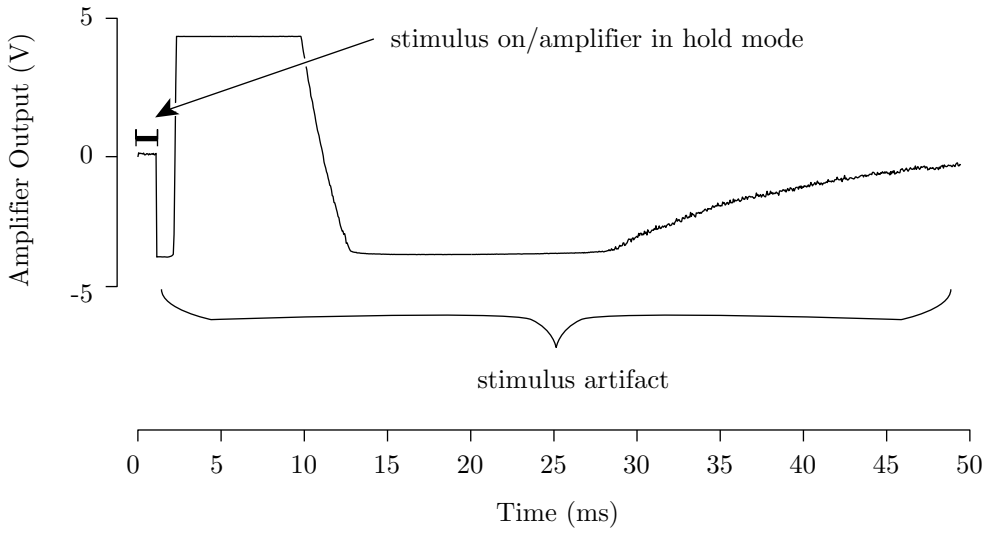

Figure C.2: Stimulus artifact, with sample and hold circuit activated.

of the preamplifier outputs, however, revealed that the preamplifiers did not saturate even when long stimulus artifacts were observed. Hence the long artifact must have been present at the preamplifier input.

Each preamplifier has a .01μF capacitor at its input (see Figure B.13) which might contribute to the artifact. These capacitors prevent DC bias currents—needed by the AD711 op-amps' JFET inputs–from flowing through the electrodes, and also to minimize offset drift. In a few tests a MOSFET input device (LMC6081) was used instead of the AD711, and a direct connection was made from the recording electrode to the op-amp input. Stimulus artifacts were not substantially reduced, indicating that the input capacitor was not a primary contributor.

C.3 Stimulator-amplifier coupling

Stimulators are used to create electric fields in biological tissues, typically with the intention to alter the membrane potentials of neurons. But these fields also produce voltage drops across the inputs to neural response amplifiers, even when the stimulator and amplifier are powered from isolated supplies. This unintended and undesirable effect provides the simplest explanation for stimulus artifacts.

Artifacts can also be caused by currents flowing in parasitic coupling paths be-

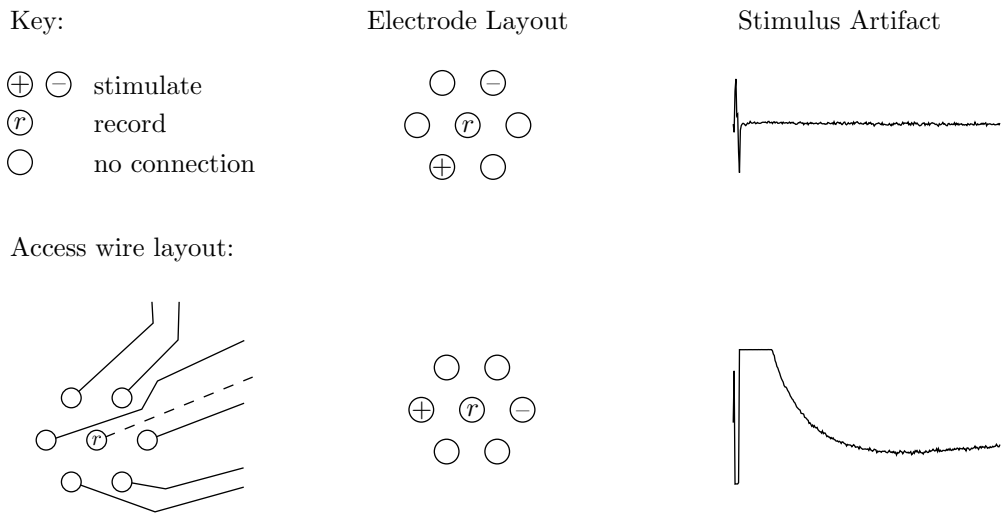

Figure C.3: Stimulus artifacts (right column) for two bipolar stimulating pairs symmetrically arranged with respect the the recording electrode (middle column). The horizontal and vertical scales are the same for the two artifacts, which were both recorded at electrode r.

tween the stimulating and recording circuits (McGill et al., 1982; Ranck, 1981), as appears to have been the case in the measurements of Figure C.3. The Figure depicts two measurements of the stimulus artifact, each using a unique pair of stimulating electrodes. The stimulus artifacts recorded at electrode r (measured with respect to a distant ground) were substantially different despite the symmetric layout of the stimulating bipolar electrode pairs with respect to the recording electrode.

Though the exposed electrodes were laid out symmetrically, the wires which provided access to them were not. As shown in the lower left of Figure C.3, some stimulating electrode access wires (solid) were closer to the recording electrode wire (dashed) than others. When the artifact was largest, the stimulating electrode wires were closest to the recording electrode wire.

This observation gave rise to the hypothesis that stimulus artifacts were produced by leakage currents flowing between the stimulating and recording electrode wires. Additional measurements supported this hypothesis. For example, shielding a recording electrode's access wires led to a dramatic reduction in the strength of the artifact. This shielding experiment is described in Figure C.4. Also, a SPICE model incorpo-

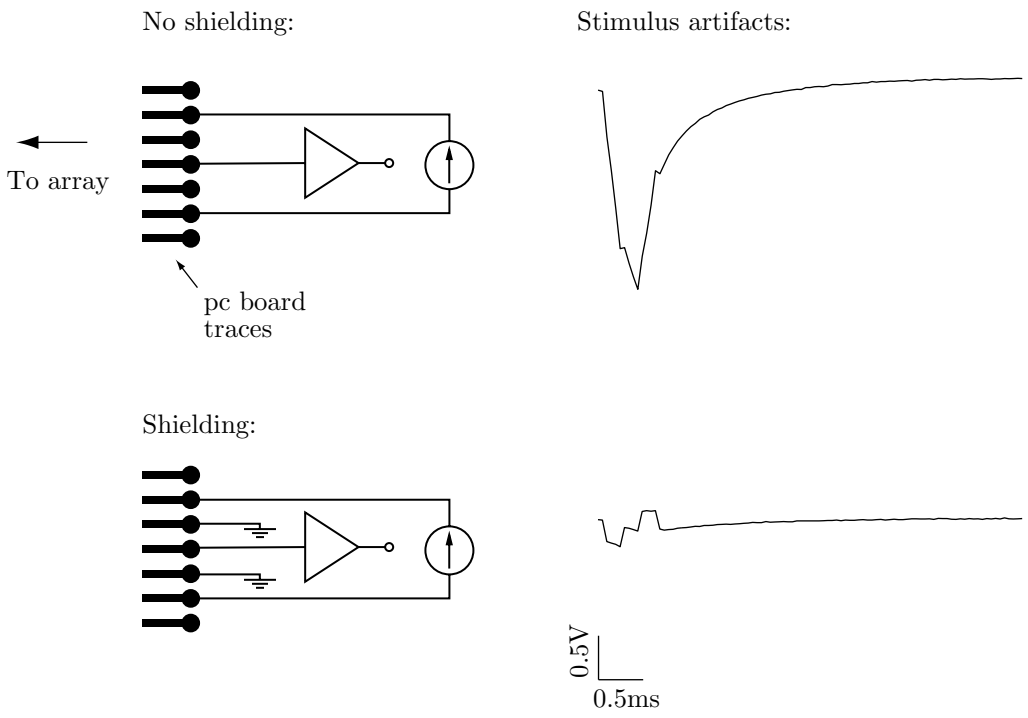

Figure C.4: Stimulus artifacts with and without shielding of the recording electrode. Shielding was achieved by connecting the PC board wires adjacent to the recording electrode wire to the recording ground (earth). These PC board wires map to wires on the electrode array as described in Section 2.3.3. Note that the shielding could have also altered the field distribution in the medium, though this effect should have been limited since the stimulator was isolated from the recording ground.

rating the hypothesized leakage pathways provided a reasonably accurate prediction of the measured artifact, as shown in Figure C.5b. The simulated artifact tracks the measured artifact quite well during the stimulus—a 200μs per phase biphasic pulse pair with an intra-phase delay of 200μs (not shown)—but overshoots the baseline (and perhaps decays back to zero) more rapidly than the measured artifact during the 1-5ms interval.

The general layout of the circuit model appears in Figure C.5a. The parasitic leakage paths between wires for each of the stimulating electrodes (B5 and A2 in the Figure) and the recording electrode (B6) were characterized by placing a drop of medium on the polyimide above the wires, being careful not to immerse the exposed electrode surfaces. Small sinewaves between 1kHz and 100kHz were applied, and the resulting data qualitatively fit to a parallel RC model for the wet polyimide. The bathing medium assumed to be isopotential.

Each electrode impedance was modeled by an access resistance in series with a parallel RC representing the electrode-electrolyte interface. The component values were determined by measuring the load voltage as a 2ms step of current was injected through a pair of electrodes. A full schematic of the SPICE model circuit, incorporating the electrode impedances and the current source output network (see Figure B.7) is shown in Figure C.6.

It is interesting to note that the circuit topology of Figure C.5a will produce no artifact if the leak impedances at the top and bottom of the circuit are equal. This a consequence of the symmetry of the circuit: if leak impedances are equal and the B5 and A2 impedances are equal, then no potential drop will be produced across the B6 impedance. One might be able to make practical use of this observation if equal electrode and leakage impedances could be assured, and if the shunt currents in the leak paths were acceptably low. I did not attempt this approach, since there was a straightforward way to raise the leak impedances.

The arrays used in the measurements above had a 1μm thick layer of polyimide insulation. This thickness was raised to 10μm to decrease the capacitance of the insulating layer. Furthermore a silicon nitride layer was added (see Figure 2.4) to provide a barrier to ionic (resistive) current flow. These changes substantially raised the leak impedances, which were so large as to be indistinguishable from the driving impedance of the dry array (i.e. no fluid to provide a leak path) in parallel with a 10x scope probe (9MΩ || 20pF). More importantly, the changes led to a substantial decrease in the artifact duration, as illustrated in Figure C.7.

With the improved isolation, stimulus artifacts usually ended abruptly when the stimulus was over. At least in salt water. Unfortunately, the artifacts grew again when a retina was placed on the array. To further reduce coupling in the tissue, the electrodes were divided into separate clusters for stimulation and recording which were spaced several hundred microns apart (see Figure 2.2). Care was also taken to run the access wires for stimulation and recording to opposite edges of the array, to reduce the chances for any additional leakage currents to flow between these.

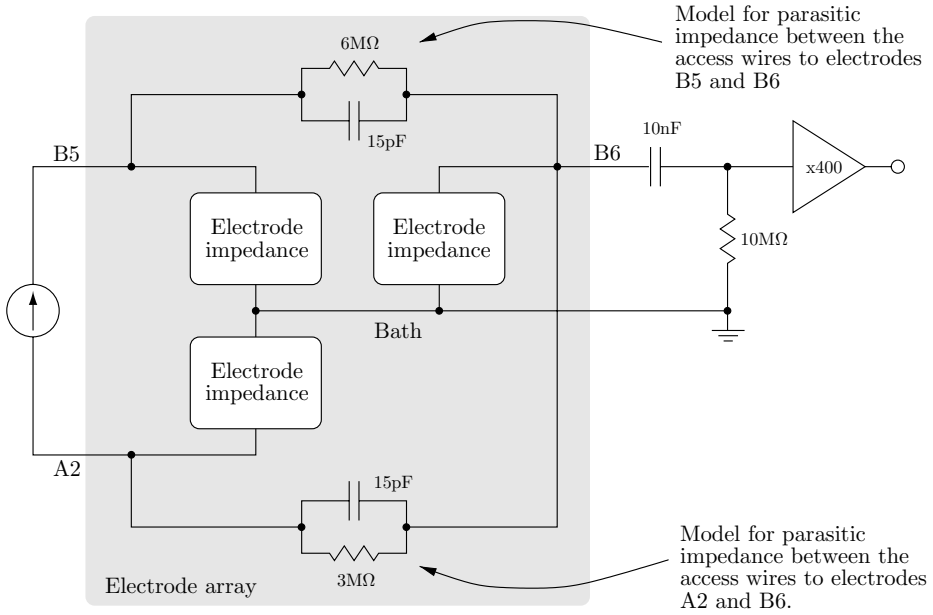

(a)

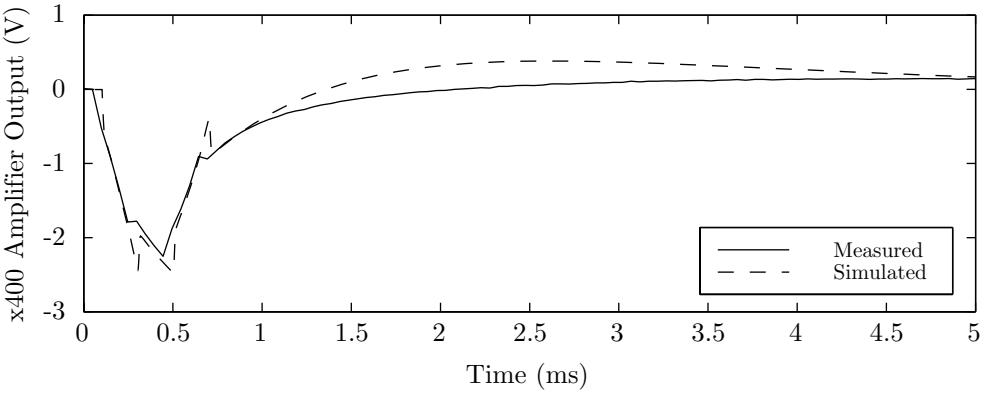

(b)

Figure C.5: A SPICE simulation reproduces the stimulus artifact to a fair degree. (a) Simplified circuit; (b) Comparison of simulated and measured artifacts. For these measurements the signal was examined prior to the final high pass filter and 25.4x gain (see Figure B.16), to avoid artifact contributions from amplifier saturation or filter transients.

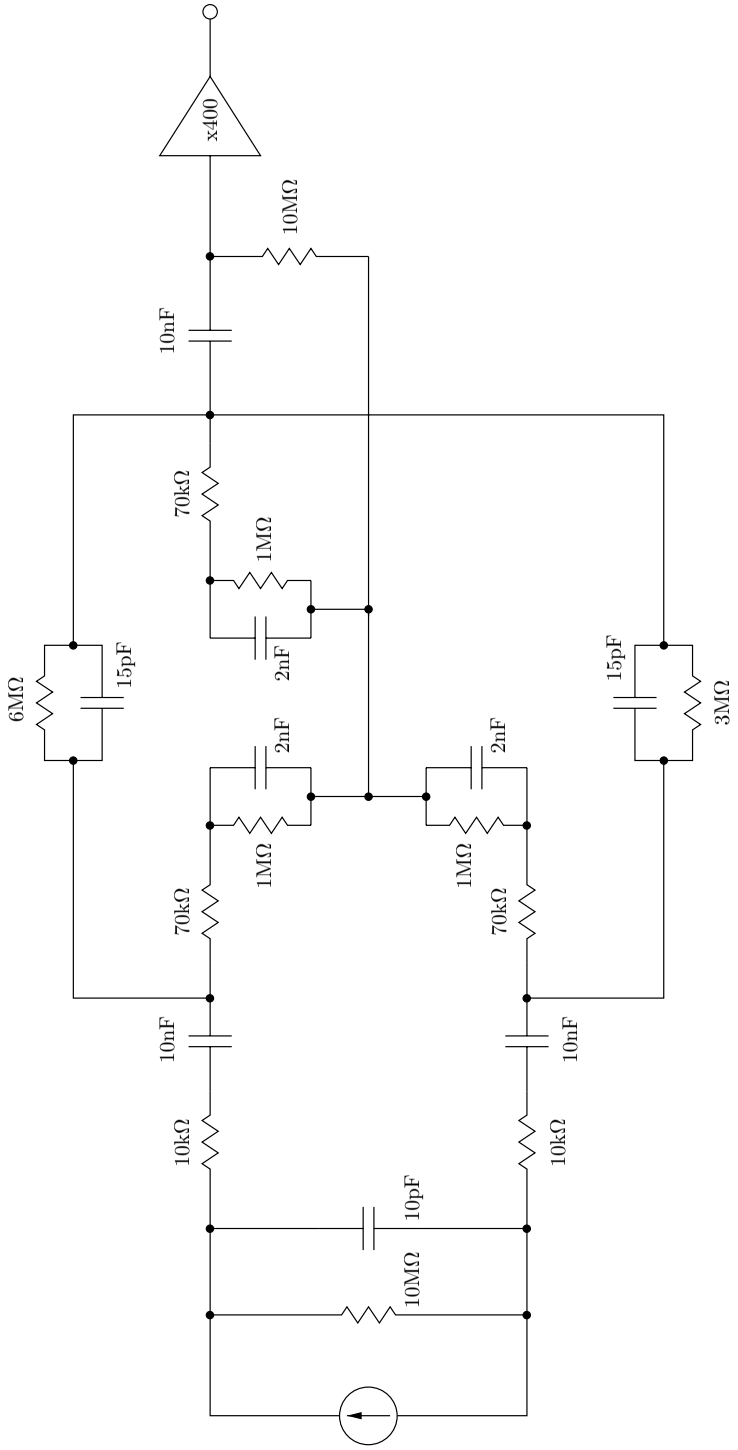

Figure C.6: Spice model for stimulus artifacts.

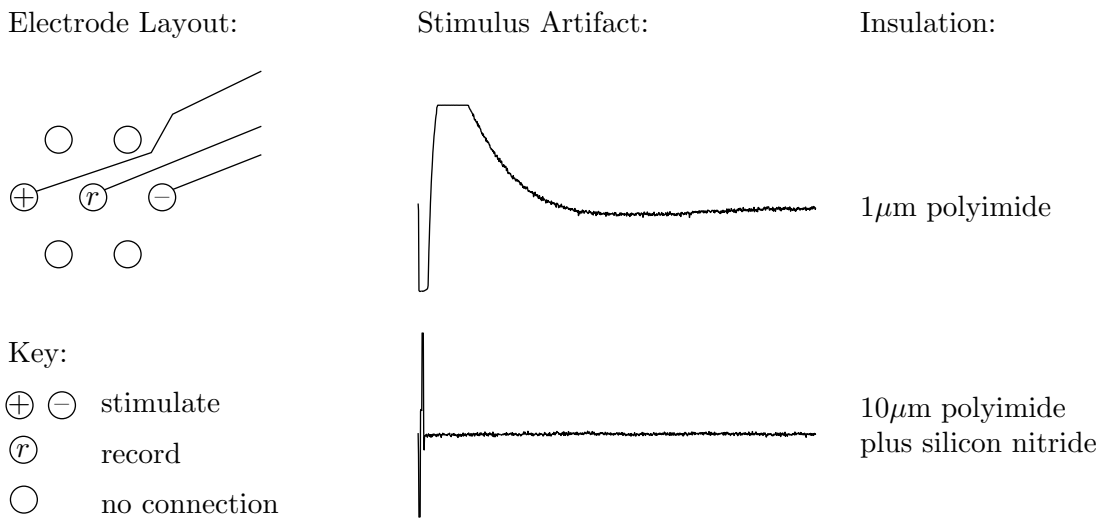

Figure C.7: Stimulus artifacts with old and new array insulation.

C.4 Stimulator considerations

C.4.1 Offsets and supply coupling

A simple control measurement was often performed, wherein artifacts were measured while applying a zero-amplitude stimulus. Sometimes, surprisingly, substantial artifacts were recorded under these conditions. Two remedies helped reduce artifacts in these cases. First, offsets in the current source—which can result in steps of stimulation current when the stimulation waveform is set to zero—were nulled using the potentiometers on the stimulator (see Section B.2.3). Second, these artifacts could sometimes be reduced by running the preamplifiers from a different power supply from the one used to for the remaining non-isolated instruments (i.e. the response amplifier and the non-isolated side of the stimulator). Though both supplies shared a common ground, it is possible that the change reduced coupling through positive and/or negative supply rails.

C.4.2 Series coupling capacitors

The stimulator has capacitors in series with its outputs to protect electrodes from DC current. If the stimulation current waveform is not charge-balanced, there will be charge left on these series coupling capacitors at the end of the stimulus. This charge will decay through a loop consisting of the two series capacitors, the electrodes, and the output impedance of the current source (see Section B.6.2). The dynamics of the charge decay are potentially quite slow, and the discharging current functions like additional stimulation current. Might this charge decay account for the slowly decaying artifact?

Generally speaking, no, since charge-balanced pulses were almost always used. In a few cases a more direct test was performed wherein the capacitors were short circuited. The change had no effect on the stimulus artifact. Occasionally monophasic pulses were applied, and artifacts were usually larger for these than for charge-balanced biphasic pulses. The series coupling capacitors may played a significant role under these conditions. On the other hand, the capacitance of the stimulating electrodes themselves must also be reckoned with.

C.5 Electrode capacitance

C.5.1 Stimulating electrodes

Because stimulating electrodes have capacitive as well as resistive properties (Kovacs, 1994) they too can accumulate charge during stimulation. If any charge is left on the electrode capacitance following stimulation, it will decay away slowly across the electrode resistance.

The simple circuit model in Figure C.8 illustrates this idea. With the stimulator in turned on (Figure C.8a) current passes through the electrode and charges the electrode capacitance C_e. Even when (in fact, *particularly* when) a charge-balanced stimulation waveform is used there will be net charge on C_e at the end of stimulation, due to leakage through the electrode resistance R_e. This net charge then decays through the electrode resistance after the stimulator has been turned off, as shown in Figure C.8b.

This decaying charge can be observed by closing a switch across the electrodes immediately following stimulation, as in Figure C.8c. If the measuring resistance R_m is smaller than the electrode resistance R_e, closing the switch provides an effective shunt path for discharging of the electrode capacitance. Figure C.8 shows the results of making such an observation.

The decaying charge creates electric fields in the fluid (or in parasitic pathways between stimulator and amplifier) which may be picked up as artifact. This this contribution to the artifact might be reduced by shorting the stimulating electrodes to each other following stimulation, as in Figure C.8 (though care should be taken

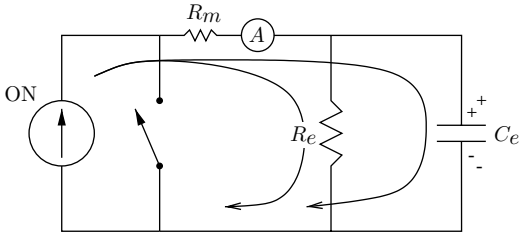

(a) Leaky charging of the electrode during stimulation.

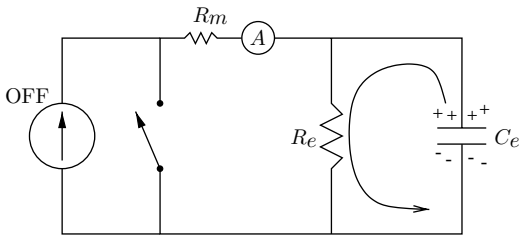

(b) Discharging through electrode resistance after stimulator has turned off.

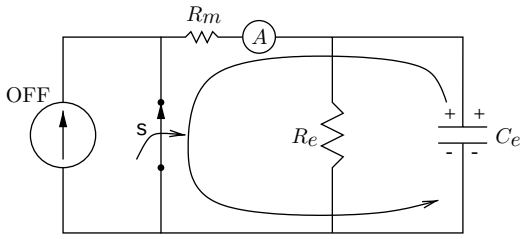

(c) Discharging through measuring resistance after switch closes.

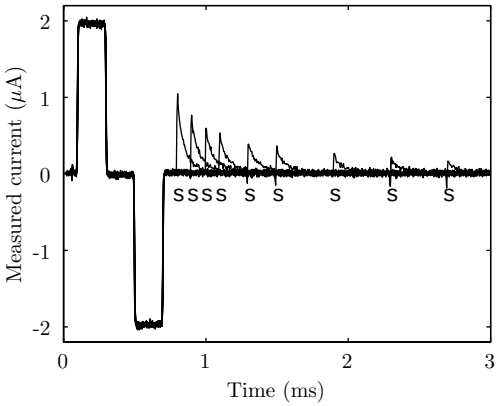

(d) Overlay of measurements with switch closed at several different times (each marked by an s). Decaying electrode charge shows up as deflections in the current coincident with the switch closings.

Figure C.8: Circuit model for and measurements demonstrating decay transients on stimulating electrodes.

not to discharge the electrodes through the stimulator's series coupling capacitors). Stimulators which do this have been reported previously (e.g. Del Pozo and Delgado (1978))), though the motivation was usually to preserve the electrodes from corrosion rather than to reduce stimulus artifacts. A related approach would be to short stimulator outputs to ground following stimulation.

In a small number of measurements these two approaches were found to lead to larger rather than smaller artifacts. It may be that DC potentials on stimulating electrodes (due to electrochemical batteries at the electrode-electrolyte interfaces) may have compounded the problem, or that other sources—that these techniques would not remedy—dominated the artifacts.

C.5.2 Recording electrodes

Recording electrodes also have capacitance and hence can also accumulate charge. Some attempts were made to use electronic switches to briefly short recording electrodes to ground following stimulation, to relieve them of any lingering charge. If decaying charge on the recording electrode was the primary source of stimulus artifacts, this technique might allow one to record undistorted nerve responses.

While simple in principle, implementation of this technique proved quite challenging and ultimately did not solve the problem. For example, the problem of switch feedthrough had to be addressed. To try and null out the channel charge, the switch was implemented with two MOSFETS—a p-channel device and an n-channel device. By design, opening or closing the switch required that the two devices be driven with opposite polarity steps, providing some cancellation of channel charge. Furthermore, the amplitude of control step on one of the devices could be manually adjusted to optimize artifact rejection. Trimpots were provided for adjustment of both the gate-to-source and gate-to-substrate voltages on this device.

Upon deployment of the switches, stimulus artifacts became time-variant. A stimulus applied at 1Hz would produce artifacts of different sizes upon each presentation. Adjusting the trimpots provided only momentary reduction of stimulus artifacts.

Then again, shorting to *ground* may not have been the best idea to begin with, since electrode-electrolyte interfaces generate a nonzero battery potential (100mV in one measurement) which can be drift-prone. Perhaps this was the source of time-varying nature of the artifact in the previously described set of measurements. A further effort was undertaken to sample the battery potential prior to stimulation and then lock the amplifier input node to this potential during stimulus application. This circuit was not successful either—artifacts still varied with time and could not be effectively nulled out.

C.6 Reducing stimulus artifacts: an overview

Though the investigations described in this appendix made possible a variety of useful measurements (see Chapters 2 and 3), they by no means solved the problem completely. For future reference, this section provides a general overview of many causes of and approaches to the problem of reducing stimulus artifacts.

C.6.1 What to look for

Two basic factors give rise to stimulus artifacts like the one in Figure C.1. First, a coupling pathway between the stimulator and recording amplifier is necessary. This might be an obvious pathway such as the tissue under study, or it might be a more subtle pathway involving power supplies or parasitic impedances between the stimulator and amplifier. Or it might be a combination of these. This first factor accounts for the part of the artifact which occurs while the stimulus is active. A second factor is required for the artifact to outlast the stimulus: the existence of one or more slowly discharging capacitances. Such capacitors might be present in the stimulator, the amplifier, or at electrode-electrolyte interfaces. Slowly unsaturating op-amps also fit into this category. The capacitors might also be part of a parasitic coupling pathway between the stimulator and amplifier.

C.6.2 What to do

1. **Minimize coupling between the stimulator and amplifier.** This can be achieved by using separate supplies and grounds for the stimulator and amplifier, keeping the amplifier input impedance as large as possible, and keeping the leads for stimulating and recording electrodes as far from one another as possible and shielded if possible. With regard to the shielding, recording electrodes should be surrounded by conductors connected to the recording ground and stimulating electrodes should be surrounded by driven shields at the same potentials.

2. **Use "subtractive" methods** There are several related approaches wherein an estimate of the artifact signal is subtracted from the response signal prior to amplification. For example, if a reasonable prediction of the stimulating field distribution can be made and/or if the experimenter has flexibility in placing recording electrodes, artifacts can sometimes be eliminated by recording differentially and placing the + and - recording electrodes at different points on an isopotential surface (McGill et al., 1982; Ranck, 1981). Another approach utilized a single electrode for stimulation and recording. To estimate the potential due to charge decay on this electrode, a second identical electrode (at a remote location in the bathing medium) was stimulated with an identical stimulus (Hentall, 1991). A third approach would be to use a computer and signal

processing to estimate the artifact, perhaps based on an average or subthreshold measurement. If the artifacts saturate the amplifier under suprathreshold conditions, it will be necessary to re-inject and subtract out a scaled version of the estimate prior to high gain amplification. If amplifiers are not saturated, all manipulations can be done directly on the amplifier output. Critical to all of these methods is to generate an estimate which is reliable and free of response components.

3. **Identify and minimize slowly discharging capacitors.** These may take the form of parasitics between stimulating and recording electrodes or be present in high-pass filters, at op-amp inputs, or at electrode-electrolyte interfaces. The parasitics can sometimes be reduced by keeping stimulating and recording leads far apart and by shielding, as described above. Op-amp input capacitances and electrode interface capacitances can sometimes be reduced through the technique of negative capacitance compensation (Crapper and Noell, 1963; Greenberg, 1998a).

4. **Prevent capacitors from acquiring charge in the first place.** Electronic switches can sometimes be used to prevent capacitors from acquiring charge during stimulation. For example, high pass filter capacitors can be protected using a sample and hold circuit, as discussed in Section C.2.2.

5. **Actively discharge capacitors.** In principle, if slowly discharging capacitors can be identified, one should be able to quickly discharge them using electronic switches. In practice, getting such circuits to work may prove challenging, especially if these capacitors reside at the input of a high gain amplifier (see Section C.5.2).

Bibliography

Ames III, A. and Masland, R. H. (1976). Responses to acetylcholine of ganglion cells in an isolated mammalian retina. *Journal of Neurophysiology*, 39(6):1220–1235.

Ames III, A. and Nesbett, F. B. (1981). In vitro retina as an experimental model of the central nervous system. *Journal of Neurochemistry*, 37(4):867–877.

Ames III, A. and Pollen, D. A. (1969). Neurotransmission in central nervous tissue: a study of isolated rabbit retina. *Journal of Neurophysiology*, 32:424–442.

Amthor, F. R., Oyster, C. W., and Takahashi, E. S. (1983). Quantitative morphology of rabbit retinal ganglion cells. *Proc. R. Soc. Lond. B*, 217:341–355.

Berson, E. L. (1993). Retinitis pigmentosa. *Investigative Ophthalmology and Visual Science*, 34(5):1659–1676.

Brindley, G. S. (1955). The site of electrical excitation of the human eye. *Journal of Physiology*, 127:189–200.

Caldwell, J. H. and Daw, N. W. (1978). New properties of rabbit retinal ganglion cells. *Journal of Physiology*, 276:257–276.

Chow, A. Y. and Chow, V. Y. (1997). Subretinal electrical stimulation of the rabbit retina. *Neuroscience Letters*, 225:13–16.

Crapper, D. R. and Noell, W. K. (1963). Retinal excitation and inhibition from direct electrical stimulation. *Journal of Neurophysiology*, 26:924–946.

Dawson, W. W. and Radtke, N. D. (1977). The electrical stimulation of the retina by indwelling electrodes. *Investigative Ophthalmology and Visual Science*, 16(3):249–252.

Doty, R. W. and Grimm, F. R. (1962). Cortical responses to local electrical stimulation of retina. *Experimental Neurology*, 5:319–334.

Eckmiller, R. (1997). Learning retina implants with epiretinal contacts. *Ophthalmic Research*, 29(5):281–9.

Freeman, J. A. (1971). An electronic stimulus artifact suppressor. *Electroencephalography and Clinical Neurophysiology*, 31:170–172.

Gernandt, B. and Granit, R. (1947). Single fibre analysis of inhibition and the polarity of the retinal elements. *Journal of Neurophysiology*, 10:295–302.

Granit, R. (1946). The distribution of excitation and inhibition in single-fibre responses from a polarized cat retina. *Journal of Physiology*, 105:45–53.

Granit, R. (1948). Neural organization of the retinal elements, as revealed by polarization. *Journal of Neurophysiology*, 11:239–251.

Greenberg, R. J. (1998a). *Analysis of Electrical Stimulation of the Vertebrate Retina – Work Towards a Retinal Prosthesis*. PhD thesis, Johns Hopkins University. Chapter 3: The target of trans-retinal electrical stimulation in frog retina—a quantitative analysis of ganglion cell response latencies.

Greenberg, R. J. (1998b). *Analysis of Electrical Stimulation of the Vertebrate Retina – Work Towards a Retinal Prosthesis*. PhD thesis, Johns Hopkins University. Chapter 4: Stimulation pulse width determines retinal element excited by electrical stimulation.

Greenberg, R. J. (1998c). *Analysis of Electrical Stimulation of the Vertebrate Retina – Work Towards a Retinal Prosthesis*. PhD thesis, Johns Hopkins University. Chapter 5: Electrode geometry design for a retinal prosthesis.

Greenberg, R. J., Velte, T. J., Humayun, M. S., Scarlatis, G. N., and Eugene de Juan, J. (1999). A computational model of electrical stimulation of the retinal ganglion cell. *IEEE Transactions on Biomedical Engineering*, 46(5):505–514.

Grumet, A. E. (1994). Extracellular electrical stimulation of retinal ganglion cells. Master's thesis, Massachusetts Institute of Technology.

Grumet, A. E., Wyatt, J. L., and Rizzo, J. F. (1998). Multi-electrode recording and stimulation of the salamander retina in vitro. *Investigative Ophthalmology and Visual Science*, 39(4):S565. (Abstract).

Hambrecht, F. T. (1990). The history of neural stimulation and its relevance to future neural prostheses. In Agnew, W. F. and McCreery, D. B., editors, *Neural Prostheses: Fundamental Studies*. Prentice Hall.

Hentall, I. D. (1991). Coincident recording and stimulation of single and multiple neuronal activity with one extracellular microelectrode. *Journal of Neuroscience Methods*, 40:181–191.

Horowitz, P. and Hill, W. (1989). *The Art of Electronics, 2nd Ed.* Cambridge University Press.

Howarth, C. I. (1954). Strength duration curves for electrical stimulation of the human eye. *The Quarterly Journal of Experimental Psychology*, 6:47–61.

Humayun, M. S., Eugene de Juan, J., Dagnelie, G., Greenberg, R. J., Propst, R. H., and Phillips, D. H. (1996). Visual perception elicited by electrical stimulation of retina in blind humans. *Archives of Ophthalmology*, 114:40–46.

Humayun, M. S., Eugene de Juan, J., Weiland, J. D., Dagnelie, G., Katona, S., Greenberg, R. J., and Suzuki, S. (1999). Pattern electrical stimulation of the human retina. *Vision Research*, 39:2569–2576.

Humayun, M. S., Propst, R., Eugene de Juan, J., McCormick, K., and Hickingbotham, D. (1994). Bipolar surface electrical stimulation of the vertebrate retina. *Archives of Ophthalmology*, 112:110–116.

Jensen, R. J., Rizzo, J. F., Grumet, A. E., Edell, D. J., and Wyatt, J. L. (1996). Single unit recording following extracellular electrical stimulation of rabbit retinal ganglion bodies. Technical Report 600, MIT Research Laboratory of Electronics.

Knighton, R. W. (1975). An electrically evoked slow potential of the frog's retina. I. properties of response. *Journal of Neurophysiology*, 38:185–197.

Kovacs, G. T. A. (1994). Introduction to the theory, design, and modeling of thin-flim microelectrodes for neural interfaces. In Stenger, D. A. and McKenna, T. N., editors, *Enabling Technologies for Cultured Neural Networks*. Academic Press.

Kuffler, S. W. (1953). Discharge patterns and functional organization of mammalian retina. *Journal of Neurophysiology*, 16:37–68.

Kuras, A. and Gutmanienė, N. (1997). Multi-channel metallic electrode for threshold stimulation of frog's retina. *Journal of Neuroscience Methods*, 75:99–102.

Loizou, P. C. (1999). Introduction to cochlear implants. *IEEE Engineering in Medicine and Biology Magazine*, 18(1):32–42.

McGill, K. C., Cummins, K. L., Dorfman, L. J., Berlizot, B. B., Luetkemeyer, K., Nishimura, D. G., and Widrow, B. (1982). On the nature and elimination of stimulus artifact in nerve signals evoked and recorded using surface electrodes. *IEEE Transactions on Biomedical Engineering*, 29(2):129–137.

McNeal, D. R. (1976). Analysis of a model for excitation of myelinated nerve. *IEEE Transactions on Biomedical Engineering*, BME-23:329–337.

Meister, M., Pine, J., and Baylor, D. A. (1994). Multi-neuronal signals from the retina: acquisition and analysis. *Journal of Neuroscience Methods*, 51:95–106.

Minzly, J., Mizrahi, J., Hakim, N., and Liberson, A. (1993). Stimulus artefact suppressor for EMG recording during FES by a constant-current stimulator. *Medical and Biological Engineering and Computing*, 31:72–75.

Mittman, S., Taylor, W. R., and Copenhagen, D. R. (1990). Concomitant activation of two types of glutamate receptor mediates excitation of salamander retinal ganglion cells. *Journal of Physiology*, 428:175–197.

Miyachi, E., Takahashi, K., and Murakami, M. (1984). Electrically evoked calcium responses in rods of the frog retina. *Japanese Journal of Physiology*, 34:307–318.

Molotchnikoff, S. (1976). Transient responses of rabbit retinal ganglion cells to photic and electrical stimuli. *The Canadian Journal of Neurological Sciences*, 3(1):73–79.

Molotchnikoff, S. and Lachapelle, P. (1978). Lateral geniculate cell responses to electrical stimulation of the retina. *Brain Research*, 152:81–95.

Morrison, R. (1986). *Grounding and Shielding Techniques in Instrumentation, 3rd Ed.* John Wiley & Sons, Inc.

Murakami, M., Shimoda, Y., Nakatani, K., Miyachi, E., and Watanabe, S. (1982). Gaba-mediated negative feedback from horizontal cells to cones in carp retina. *Japanese Journal of Physiology*, 32:911–926.

Normann, R. A., Maynard, E. M., Rousche, P. J., and Warren, D. J. (1999). A neural interface for a cortical vision prosthesis. *Vision Research*, 39(15):2577–2587.

Ogden, T. E. and Brown, K. T. (1964). Intraretinal responses of the cynamolgus monkey to electrical stimulation of the optic nerve and retina. *Journal of Neurophysiology*, 27:682–705.

Ogden, T. E. and Ito, H. (1971). Avian retina. II. an evaluation of retinal electrical anisotropy. *Journal of Neurophysiology*, 34:367–373.

Peichl, L., Buhl, E. H., and Boycott, B. B. (1987). Alpha ganglion cells in the rabbit retina. *Journal of Comparative Neurology*, 263:25–41.

Pickard, R. S. (1979). A review of printed circuit microelectrodes and their production. *Journal of Neuroscience Methods*, 1:301–318.

Plonsey, R. (1969). *Bioelectric Phenomena*. McGraw Hill, Inc.

Plonsey, R. and Altman, K. W. (1988). Electrical stimulation of excitable cells – a model approach. *Proceedings of the IEEE*, 76(9):1122–1128.

Potts, A. M. and Inoue, J. (1970). The electrically evoked response of the visual system (eer). III. further contribution to the origin of the eer. *Investigative Ophthalmology and Visual Science*, 9(10):814–819.

Pozo, F. D. and Delgado, J. M. R. (1978). Hybrid stimulator for chronic experiments. *IEEE Transactions on Biomedical Engineering*, 25(1):92–94.

Ranck, Jr., J. B. (1975). Which elements are excited in electrical stimulation of mammalian central nervous system: a review. *Brain Research*, 98:417–440.

Ranck, Jr., J. B. (1981). Extracellular stimulation. In Patterson, M. M. and Kesner, R. P., editors, *Electrical Stimulation Research Techniques*. Academic Press.

Ranjan, R. and Thakor, N. V. (1995). Electrical stimulation of cardiac myocytes. *Annals of Biomedical Engineering*, 23:812–821.

Rattay, F. (1986). Analysis of models for external stimulation of axons. *IEEE Transactions on Biomedical Engineering*, BME-33(10):974–977.

Regehr, W. G., Pine, J., Cohan, C. S., Mischke, M. D., and Tank, D. W. (1989). Sealing cultured invertebrate neurons to embedded dish electrodes facilitates long-term stimulation and recording. *Journal of Neuroscience Methods*, 30:91–106.

Rizzo, J. F., Grumet, A. E., Edell, D. J., Wyatt, J. L., and Jensen, R. J. (1997). Single-unit recordings following extracellular stimulation of retinal ganglion cell axons in rabbits. *Investigative Ophthalmology and Visual Science*, 38(4):S40. (Abstract) Poster may be viewed online at `http://rleweb.mit.edu/retina/poster9.html`.

Rizzo, J. F. and Wyatt, J. L. (1997). Prospects for a visual prosthesis. *The Neuroscientist*, 3(4):251–262.

Robblee, L. S. and Rose, T. L. (1990). Electrochemical guidelines for selection of protocols and electrode materials for neural stimulation. In Agnew, W. F. and McCreery, D. B., editors, *Neural Prostheses: Fundamental Studies*. Prentice Hall.

Roby, R. J. and Lettich, E. (1975). A simplified circuit for stimulus artifact suppression. *Electroencephalography and Clinical Neurophysiology*, 39:85–87.

Rodieck, R. W. (1973). *The vertebrate retina: principles of structure and function*. W.H. Freeman and Company.

Rubinstein, J. T. and Spelman, F. A. (1988). Analytical theory for extracellular electrical stimulation of nerve with focal electrodes. I. passive unmyelinated axon. *Biophysical Journal*, 54:975–981.

Rushton, W. A. H. (1927). The effect upon the threshold for nervous excitation of the length of nerve exposed, and the angle between current and nerve. *Journal of Physiology*, 63:357–377.

Santos, A., Humayun, M. S., Eugene de Juan, J., Greenberg, R. J., Marsh, M. J., Klock, I. B., and Milam, A. H. (1997). Preservation of the inner retina in retinitis pigmentosa. *Archives of Ophthalmology*, 115:511–515.

Sherman-Gold, R., editor (1993). *The Axon Guide for Electrophysiology and Biophysics Laboratory Techniques*. Axon Instruments, Inc.

Stanford, L. R. (1987). Conduction velocity variations minimize conduction time differences among retinal ganglion cell axons. *Science*, 238:358–360.

Stone, J. L., Barlow, W. E., Humayun, M. S., Eugene de Juan, J., and Milam, A. H. (1992). Morphometric analysis of macular photoreceptors and ganglion cells in retinas with retinitis pigmentosa. *Archives of Ophthalmology*, 110:1634–1639.

Tehovnik, E. J. (1996). Electrical stimulation of neural tissue to evoke behavioral responses. *Journal of Neuroscience Methods*, 65:1–17.

Toyoda, J. and Fujimoto, M. (1984). Application of transretinal current stimulation for the study of bipolar-amacrine transmission. *Journal of General Physiology*, 84:915–925.

Trifonov, Y. A. and Byzov, A. L. (1977). The interaction in photoreceptor synapses revealed in experiments with polarization of horizontal cells. In Barlow, H. and Fatt, P., editors, *Vertebrate Photoreception*. Academic Press.

Tung, L., Sliz, N., and Mulligan, M. R. (1991). Influence of electrical axis of stimulation on excitation of cardiac muscle cells. *Circulation Research*, 69(3):722–730.

Vaney, D. I. (1980). A quantitative comparison between the ganglion cell populations and axonal outflows of the visual streak and periphery of the rabbit retina. *Journal of Comparative Neurology*, 189:215–233.

Velte, T. J. and Masland, R. H. (1999). Action potentials in the dendrites of retinal ganglion cells. *Journal of Neurophysiology*, 81:1412–1417.

Warman, E. N., Grill, W. M., and Durand, D. (1992). Modeling the effects of electric fields on nerve fibers: determination of excitation thresholds. *IEEE Transactions on Biomedical Engineering*, 39(12):1244–1254.

Weiss, T. F. (1996). *Cellular Biophysics, Volume 2: Electrical Properties*. The MIT Press.

Woodbury, J. W. (1960). Potentials in a volume conductor. In Ruch, T. and Fulton, J., editors, *Medical physiology and biophysics, 18th ed.* WB Saunders Company.

Wyatt, J. L. and Rizzo, J. F. (1996). Ocular implants for the blind. *IEEE Spectrum*, 33:47–53.

Zrenner, E., Stett, A., Weiss, S., Aramant, R. B., Guenther, E., Kohler, K., Miliczek, K. D., Zeiler, M., and Haemmerle, H. (1999). Can subretinal microphotodiodes successfully replace degenerated photoreceptors? *Vision Research*, 39(15):2555–2567.